The Astronomical Journal, 166:225 (18pp), 2023 December https://doi.org/10.3847/1538-3881/ad0135

Verification of Gaia Data Release 3 Single-lined Spectroscopic Binary Solutions With Three Transiting Low-mass Secondaries

Stephen P. Schmidt[1], Kevin C. Schlaufman[1,2], Keyi Ding (丁可怿)[1], Samuel K. Grunblatt[1], Theron Carmichael[3], Allyson Bieryla[4], Joseph E. Rodriguez[5], Jack Schulte[5], Noah Vowell[5], George Zhou[6], Samuel N. Quinn[4], Samuel W. Yee[7], Joshua N. Winn[7], Joel D. Hartman[7], David W. Latham[4], Douglas A. Caldwell[8,9], M. M. Fausnaugh[10,11], Christina Hedges[12,13], Jon M. Jenkins[9], Hugh P. Osborn[10,14], and S. Seager[10,15,16]
[1] William H. Miller III Department of Physics and Astronomy, Johns Hopkins University, 3400 N Charles Street, Baltimore, MD 21218, USA; sschmi42@jh.edu
[2] Carnegie Institution for Science Earth & Planets Laboratory, 5241 Broad Branch Road NW, Washington, DC 20015, USA
[3] Institute for Astronomy, University of Edinburgh, Royal Observatory, Blackford Hill, Edinburgh, EH9 3HJ, UK
[4] Center for Astrophysics | Harvard & Smithsonian, 60 Garden Street, Cambridge, MA 02138, USA
[5] Center for Data Intensive and Time Domain Astronomy, Department of Physics and Astronomy, Michigan State University, East Lansing, MI 48824, USA
[6] Centre for Astrophysics, University of Southern Queensland, West Street, Toowoomba, QLD 4350, Australia
[7] Department of Astrophysical Sciences, Princeton University, 4 Ivy Lane, Princeton, NJ 08544, USA
[8] SETI Institute, Moffett Field, Mountain View, CA, 94035, USA
[9] NASA Ames Research Center, Moffett Field, CA 94035, USA
[10] Department of Physics and Kavli Institute for Astrophysics and Space Research, Massachusetts Institute of Technology, Cambridge, MA 02139, USA
[11] Department of Physics & Astronomy, Texas Tech University, Lubbock, TX 79410-1051, USA
[12] University of Maryland, Baltimore County, 1000 Hilltop Circle, Baltimore, MD 21250, USA
[13] NASA Goddard Space Flight Center, 8800 Greenbelt Road, Greenbelt, MD 20771, USA
[14] NCCR/Planet-S, Universität Bern, Gesellschaftsstrasse 6, 3012 Bern, Switzerland
[15] Department of Earth, Atmospheric and Planetary Sciences, Massachusetts Institute of Technology, Cambridge, MA 02139, USA
[16] Department of Aeronautics and Astronautics, MIT, 77 Massachusetts Avenue, Cambridge, MA 02139, USA
Received 2023 August 2; revised 2023 October 5; accepted 2023 October 6; published 2023 November 6

Abstract

While secondary mass inferences based on single-lined spectroscopic binary (SB1) solutions are subject to $\sin i$ degeneracies, this degeneracy can be lifted through the observations of eclipses. We combine the subset of Gaia Data Release 3 SB1 solutions consistent with brown dwarf-mass secondaries with the Transiting Exoplanet Survey Satellite (TESS) Object of Interest (TOI) list to identify three candidate transiting brown dwarf systems. Ground-based precision radial velocity follow-up observations confirm that TOI-2533.01 is a transiting brown dwarf with $M = 72^{+3}_{-3}\,M_{\rm Jup} = 0.069^{+0.003}_{-0.003}\,M_{\odot}$ orbiting TYC 2010-124-1 and that TOI-5427.01 is a transiting very low-mass star with $M = 93^{+2}_{-2}\,M_{\rm Jup} = 0.088^{+0.002}_{-0.002}\,M_{\odot}$ orbiting UCAC4 515-012898. We validate TOI-1712.01 as a very low-mass star with $M = 82^{+7}_{-7}\,M_{\rm Jup} = 0.079^{+0.007}_{-0.007}\,M_{\odot}$ transiting the primary in the hierarchical triple system BD+45 1593. Even after accounting for third light, TOI-1712.01 has a radius nearly a factor of 2 larger than predicted for isolated stars with similar properties. We propose that the intense instellation experienced by TOI-1712.01 diminishes the temperature gradient near its surface, suppresses convection, and leads to its inflated radius. Our analyses verify Gaia DR3 SB1 solutions in the low Doppler semiamplitude limit, thereby providing the foundation for future joint analyses of Gaia radial velocities and Kepler, K2, TESS, and PLAnetary Transits and Oscillations light curves for the characterization of transiting massive brown dwarfs and very low-mass stars.

Unified Astronomy Thesaurus concepts: Brown dwarfs (185); Eclipsing binary stars (444); Substellar companion stars (1648); Spectroscopic binary stars (1557); Stellar radii (1626); Trinary stars (1714); Low mass stars (2050)

1. Introduction

While isochrones can be used to infer the masses and radii of isolated low-mass stars and brown dwarfs, the theoretical models underlying those isochrones have difficulties reproducing the measured masses and radii of such objects (Kraus et al. 2011; Birkby et al. 2012). On the other hand, the minimum masses of the secondary stars and brown dwarfs in single-lined spectroscopic binary systems (SB1s) can be measured relative to the masses of the primaries in such systems. If the photospheres of the primaries in such systems are much, much hotter than the temperatures of the secondaries' "night" sides and the secondaries have significantly smaller radii (both of which apply for the lowest-mass stellar secondaries), then the eclipses of such systems can be treated like the transits and occultations of exoplanet systems. In that case, the depth of an eclipse of the primary by the secondary can be used to measure the radius of the low-mass secondary relative to the radius of the primary. The eclipsing nature of such a system lifts the $\sin i$ degeneracy of an SB1 solution as well. If the primary is a Sun-like star, then isochrone-inferred masses and radii can be both accurate and precise. Consequently, a homogeneous analysis of a large sample of transiting single-lined spectroscopic binaries would be a powerful way to infer accurate and precise masses and radii for a large population of low-mass stars and brown dwarfs.

Gaia Data Release (DR) 3's nonsingle stars catalog (Pourbaix et al. 2022; Gaia Collaboration et al. 2023a; Babusiaux et al. 2023; Katz et al. 2023) presented a list of 181,327 single-lined spectroscopic binary solutions. This

collection of SB1s is almost 2 orders of magnitudes larger than previous catalogs (e.g., Pourbaix et al. 2004). Of these solutions, 32,455 have Sun-like primaries (F5V through K5V according to Pecaut & Mamajek 2013) based on absolute Gaia G-band magnitudes and effective temperatures $T_{\rm eff}$ from Gaia DR3's astrophysical parameters data product (Creevey et al. 2023; Fouesneau et al. 2023). Of these, 2490 secondaries have minimum masses in the brown dwarf regime defined by an upper mass cutoff of 78.5 Jupiter masses (Chabrier et al. 2023). Because of Gaia's limited time baseline and Doppler precision, these systems usually have short periods and relatively high transit probabilities. These SB1 solutions have been validated down to the brown dwarf-mass regime (Gaia Collaboration et al. 2023b). The infrequent sampling of light curves based on Gaia photometry leaves them insensitive to all but the shortest-period eclipsing systems.

NASA's Transiting Exoplanet Survey Satellite (TESS) mission has observed most of the sky in search of exoplanets and other transiting objects (Ricker et al. 2014). TESS light curves have been exhaustively searched for candidate transiting planets (Guerrero et al. 2021). Now in its Second Extended Mission, TESS data has led to the discovery of thousands of eclipsing binaries (Prša et al. 2022) and over a dozen transiting very-low-mass stars and brown dwarfs (e.g., Grieves et al. 2021; Carmichael et al. 2022; Psaridi et al. 2022; Lin et al. 2023; Vowell et al. 2023). The population of TESS-discovered eclipsing or transiting systems is biased toward periods shorter than about 10 days due to TESS's observing strategy and the smaller transit probabilities of systems with longer periods.

The combination of Gaia SB1 solutions and TESS light curves would be a powerful resource for the accurate and precise characterization of low-mass stars and brown dwarfs. In this article, we seek out systems with Gaia SB1 solutions consistent with brown dwarf-mass secondaries that have also been observed by TESS to transit their primaries. We identify three such systems for which the SB1 period is well matched by the TESS-inferred period: BD+45 1593 (TOI-1712), TYC 2010-124-1 (TOI-2533), and UCAC4 515-012898 (TOI-5427). Our ground-based follow-up analysis subsequently reveals that BD+45 1593 Ab (TOI-1712.01) is a very-low-mass star transiting the primary in a hierarchical triple, TYC 2010-124-1 b (TOI-2533.01) is a transiting brown dwarf, and UCAC4 515-012898 b (TOI-5427.01) is a transiting very-low-mass star. We describe the initial identification of these three objects as potential brown dwarfs in Section 2. We describe our follow-up observations for the systems and our subsequent analysis to confirm or validate the three objects in Section 3. We discuss the implications of these discoveries in Section 4 and summarize our conclusions in Section 5.

2. Candidate Brown Dwarf Identification

We first cross-match Gaia DR3's nonsingle stars product with the TESS object of interest (TOI) catalog and the TESS eclipsing binary catalog (Prša et al. 2022). We next focus on systems where the orbital period from the Gaia SB1 solution is within 0.3% of the period found by TESS. We then use the binary mass function

$$f(M) = \frac{M_2^3 \sin^3 i}{(M_1 + M_2)^2} = \frac{P K_1^3}{2\pi G}(1 - e^2)^{3/2}, \quad (1)$$

in the $M_2 \ll M_1$ limit to calculate a preliminary minimum mass for each secondary:

$$\frac{M_2 \sin i}{M_{\rm Jup}} = \left(\frac{K_1}{28.4329 \text{ m s}^{-1}}\right)\sqrt{1 - e^2}\,(M_1)^{2/3}P^{1/3}. \quad (2)$$

The inputs to Equation (2) are a primary mass M_1 in Solar masses from Gaia's Final Luminosity Age Mass Estimator (FLAME) and a system's Gaia DR3 SB1 solution orbital parameters Doppler semiamplitude K_1 in meters per second and period P in years. In cases in which a FLAME-derived mass is unavailable, we use the primary mass from the TESS Follow-up Observing Program (TFOP) instead. For systems in which secondary mass is comparable to that of a brown dwarf, we refine our preliminary mass estimates by calculating more precise stellar parameters for the primary.

This procedure yields three systems with candidate brown dwarfs: BD+45 1593 (Gaia DR3 917823348536224768/TOI-1712), TYC 2010-124-1 (Gaia DR3 1259922196651254272/TOI-2533), and UCAC4 515-012898 (Gaia DR3 3341401062125577088/TOI-5427). We illustrate these systems in Figure 1 and describe them in detail below. These SB1 solutions are based on Gaia $R \approx 11$, 500 Radial Velocity Spectrometer (RVS) spectra that cover the wavelength range 846 nm $\lesssim\lambda\lesssim$870 nm (Katz et al. 2023). The SB1 solutions for BD+45 1593 used 18 "good" radial velocity (RV) measurements, TYC 2010-124-1 used 47 "good" RV measurements, and UCAC4 515-012898 used 25 "good" RV measurements. We refer to these systems by their TESS Object of Interest designations TOI-1712, TOI-2533, and TOI-5427 in the context of analyses based on data sourced solely from TESS or TFOP. In all other contexts, we refer to these systems by their Simbad designations BD+45 1593, TYC 2010-124-1, and UCAC4 515-012898.

TOI-1712 and TOI-5427 were discovered by the TESS Science Office, while TOI-2533 was first discovered by Rafael Brahm. TOI-2533 then became a community TESS object of interest (CTOI), and later was adopted as a TOI by the TESS Science Office. TOI-1712 and TOI-2533 were identified by the TESS quick-look pipeline (QLP; Huang et al. 2020a, 2020b), while TOI-5427 was identified by the TESS QLP Faint-star Search (Kunimoto et al. 2022). We give in Table 1 the details of the TESS observations of the three objects. For stars like the primaries in these systems that were not allocated postage stamps, TESS collected observations with a 30 minute cadence during its Prime Mission and a 10/2 minute cadence during its First/Second Extended Mission.

Because of TESS's large pixels, third light can make it difficult to interpret transit depths directly as secondary-to-primary radius ratios. To investigate the possibility of third light in these systems, we do two things. We first confirm that the TESS contamination ratios[17] are small for each system: 0.00054 for TOI-1712, 0.039224 for TOI-2533, and 0.263055 for TOI-5427. We next use the high spatial resolution Gaia DR3 source catalog and the plotting function within the `giants` pipeline (Grunblatt et al. 2022a; Saunders et al. 2022) to show that there are no bright sources within the TESS `lightkurve`-generated (Collaboration et al. 1812) full-frame

[17] TESS contamination ratios are given as the column `contratio` in the TESS Input Catalog (Stassun et al. 2019).

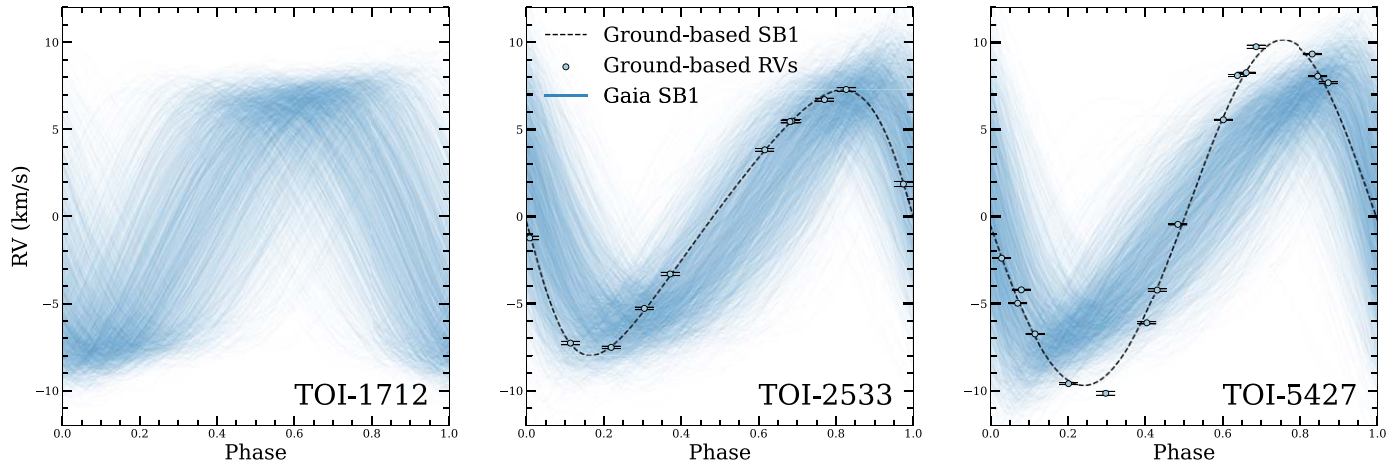

Figure 1. Doppler curves for BD+45 1593, TYC 2010-124-1, and UCAC4 515-012898 based on their Gaia DR3 and ground-based SB1 solutions. We plot 2000 partially transparent blue lines to represent individual solutions sampled from normal distributions of the Gaia Doppler semiamplitude, eccentricity, and argument of periastron, with the standard deviation of each distribution representing the reported error on its respective parameter. Gaia's reported uncertainties on each parameter are derived from the variance-covariance matrix of the solution, but the matrix itself is not reported; we therefore do not correct for it in this plot. We plot the individual precision ground-based radial velocity measurements and their uncertainties as light blue circles with black borders and error bars. We plot the Doppler curves inferred from these data as dashed black lines. The agreement between the Gaia and precision ground-based SB1 solutions demonstrates the fidelity of the Gaia SB1 solutions at low Doppler semiamplitude.

Table 1
TESS Observations of the Three Objects

Sector	Corresponding Time Period	Cadence (Minutes)
	TOI-1712 (TIC 67926921)	
20	December 24, 2019–January 20, 2020	30
47	December 30, 2021–January 28, 2022	2, 10
	TOI-2533 (TIC 418012030)	
23	March 19, 2020–April 15, 2020	30
	TOI-5427 (TIC 52420398)	
6	December 12, 2018–January 6, 2019	30
43	September 16, 2021–October 12, 2021	10
44	October 12, 2021–November 6, 2021	10
45	November 6, 2021–December 2, 2021	10

image (FFI) point-spread function of any of these three systems (Figure 2).

We derive the fundamental and photospheric stellar parameters of BD+45 1593, TYC 2010-124-1, and UCAC4 515-012898 using the `isochrones` (Morton 2015) package to execute with `MultiNest` (Feroz & Hobson 2008; Feroz et al. 2009, 2019) a simultaneous Bayesian fit of the MIST isochrone grid (Paxton et al. 2011, 2013; Choi et al. 2016; Dotter 2016; Paxton et al. 2018, 2019; Jermyn et al. 2023) to a curated collection of data for each star. The stellar parameters derived using this approach have been shown by K. Ding et al. (2023, in preparation) to reproduce the asteroseismology-inferred masses and radii of the Kepler LEGACY Sample (Silva Aguirre et al. 2017). We fit (1) a zero-point-corrected Gaia DR3 parallax (Lindegren et al. 2021a, 2021b; Fabricius et al. 2021; Gaia Collaboration et al. 2021; Rowell et al. 2021; Torra et al. 2021), (2) Galaxy Evolution Explorer (GALEX) GUVcat_AIS NUV and FUV (Bianchi et al. 2017), Tycho-2 B_T and V_T (Høg et al. 2000), Gaia DR2 G (Gaia Collaboration et al. 2016; Arenou et al. 2018; Evans et al. 2018; Gaia Collaboration et al. 2018; Riello et al. 2018), Two Micron All-Sky Survey (2MASS) JHK_s (Skrutskie et al. 2006), and/or Wide-field Infrared Survey Explorer AllWISE W1W2W3 photometry (Wright et al. 2010; Mainzer et al. 2011), and (3) an estimated extinction value A_V based on three-dimensional reddening maps (Lallement et al. 2022; Vergely et al. 2022). GALEX photometry is unavailable for TYC 2010-124-1 and UCAC4 515-012898, and Tycho-2 photometry is unavailable for UCAC4 515-012898. We use a uniform extinction prior bounded by $A_V \pm 5\sigma_{A_V}$ and a distance prior proportional to volume bounded by the Bailer-Jones et al. (2021) lower and upper bounds on geometric distances. We report the photospheric stellar parameters in Table 3 and compare the isochrone-derived magnitudes to each star's observed magnitudes in Figure 3.

As we will show in the next section, there is evidence that BD+45 1593 is a double-lined spectroscopic binary. To determine the properties of both luminous stars in the system, we use an `isochrones` binary star model that requires both the primary and secondary to have the same age, composition, and distance. We use the full set of inputs mentioned previously. In Section 3.1, we will use the TESS T-band flux ratio that is inferred to show that the dilution of the transit in the BD+45 1593 system is small. The modeled photometry that results from the `isochrones` is consistent with the observed photometry, and this consistency supports the accuracy of the binary star model output (Figure 3).

Our isochrone analysis gives us several reasons to believe that the low-mass object in the BD+45 1593 system orbits the most massive component BD+45 1593 A. We infer T-band magnitudes $9.95^{+0.05}_{-0.03}$ for the primary BD+45 1593 A and $13.90^{+2.47}_{-1.12}$ for the secondary BD+45 1593 B. Given that the posterior-derived Gaia DR2 G magnitudes for the two stars are $10.30^{+0.05}_{-0.02}$ and $14.46^{+2.81}_{-1.25}$, we argue that this flux difference would have left Gaia insensitive to the possible RV variation of BD+45 1593 B. As we will show, the second set of lines in the Tillinghast Reflector Echelle Spectrograph reconnaissance spectra of BD+45 1593 do not move on the timescale of months. On the other hand, the agreement of the Gaia DR3 SB1 period and the transit-inferred TOI period suggests that the object of interest in the system orbits BD+45 1593 A rather than BD+45 1593 B. Therefore, we refer to the primary of this system as BD+45 1593 Aa and report its parameters in Table 3.

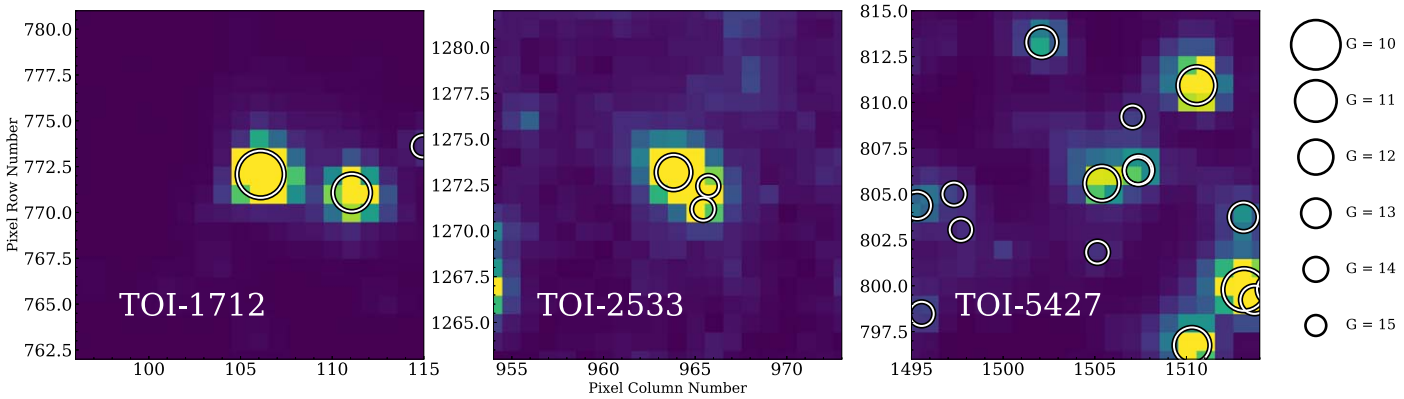

Figure 2. TESS FFI approximately 2048 × 2048 pixel postage stamps for TOI-1712, TOI-2533, and TOI-5427. TESS collected the FFI for TOI-1712 during Sector 20, the FFI for TOI-2533 during Sector 23, and the FFI for TOI-5427 during Sector 6. We center each postage stamp on the target and mark each $G < 15$ Gaia DR3 source with a white circle of radius inversely proportional to the Gaia G magnitude. These FFIs show that blending is not a concern for the light curves of the objects.

We find that BD+45 1593 Aa is a subgiant with $M_* \approx 1.63^{+0.01}_{-0.02}\,M_\odot$. It has been shown that the rotation period of a subgiant is proportional to its mass and therefore age (van Saders & Pinsonneault 2013). Assuming an aligned orbit, our inferred mass for BD+45 1593 Aa is large enough that Gaia should be able to detect the rotational broadening of its absorption lines. Indeed, the Gaia DR3 `vbroad` parameter for BD+45 1593 is 30 ± 6 km s^{-1}. We assume that all of the line broadening measured by the Gaia DR3 `vbroad` parameter is a result of rotation and use it to calculate the rotation period of BD+45 1593 Aa. We divide the isochrone-inferred circumference of BD+45 1593 Aa by its Gaia DR3 `vbroad` parameter, resulting in a rotation period $P_{\rm rot} \approx 5$ days. It is possible that angular momentum exchange between the system's revolution and the rotation of BD+45 1593 Aa would lead to its faster rotation, though in that case, one would expect that the system's orbital period $P = 3.566276 \pm 0.0000044$ days and the rotation period of the primary $P_{\rm rot} \approx 5$ days would be synchronized. The agreement between our inferred rotation period $P_{\rm rot} \approx 5$ and the van Saders & Pinsonneault (2013)-predicted slow-launch rotation period $P_{\rm slow} \approx 6$ days for a star of the mass, composition, and temperature of BD+45 1593 Aa supports our inference that BD+45 1593 Aa is massive.

3. Follow-up Observations and Analysis

3.1. Light Curve Analysis

The Box-fitting Least Squares (BLS-Kovács et al. 2002) algorithm-based transit depths reported in the TOI catalog are only indicative of true transit depths. We therefore reanalyze the TESS light curves of TOI-1712, TOI-2533, and TOI-5427 with the `juliet` Python package (Espinoza et al. 2019) to obtain more accurate and precise radius ratio posteriors for these three systems. We retrieve the light curve data products originally reduced by the TESS Science Processing Operations Center (SPOC-Jenkins et al. 2016) for the three systems from the Mikulski Archive for Space Telescopes (MAST). For each system, we use the available 30 minute cadence light curves produced from TESS Full-Frame Images by the TESS-SPOC High Level Science Products (HLSP) project (Caldwell et al. 2020). For TOI-1712, we additionally use the 2 minute cadence Presearch Data Conditioned (PDC-SAP; Smith et al. 2012; Stumpe et al. 2012, 2014) light curve from Sector 47 produced by the SPOC. Likewise, for TOI-5427 we additionally use 10 minute cadence light curves from Sectors 43, 44, and 45 also produced from TESS FFIs by the TESS-SPOC HLSP project.

We mask the transits in each light curve based on the ephemeris from the TOI catalog and use the Gaussian Process (GP) modeling tool in `juliet` to model out the stellar variability. We use a simple approximate Matern kernel for this process. For the dilution factor, we use a fixed prior at 1, for the mean out-of-transit flux we use a Gaussian prior centered at 0 with a standard deviation of 0.1, for the jitter term σ_w and amplitude of the GP $\sigma_{\rm GP}$ we use logarithmic uniform priors between 10^{-6} and 10^{6}, and for the Matern timescale of the GP $\rho_{\rm GP}$ we use a logarithmic uniform prior between 10^{-3} and 10^{3}. We plot the systems' original TESS light curves along with the Gaussian process stellar variability fit in Figure 4.

After removing stellar variability, for each light curve, we unmask the transits and use the TOI ephemeris as a prior on the `juliet` fit to extract inclination and radius ratio posteriors. We use similar priors as before, except we use the Kipping (2013) quadratic limb-darkening parameterization with `q1` and `q2` $\mathcal{U}(0, 1)$ priors appropriate for TESS. We plot in Figure 5 the detrended light curves for the systems with their transit fits, while in Figure 6 we plot the phase-folded 30 minutes-cadence light curves and transit fit for each system. We report the inclinations and radius ratios in Table 3.

3.2. Doppler Analysis

We present in Table 2 27 ground-based precision radial velocity measurements we obtained for TOI-2533 and TOI-5427. We collected 11 spectra for TOI-2533 between 2021 March 5 and 2021 April 8 using the Tillinghast Reflector Echelle Spectrograph (TRES-Fűrész 2008) on the 1.5 m Tillinghast Reflector telescope, situated on Mt. Hopkins in Arizona, USA. TRES has $R \approx 44,000$ over a wavelength range of approximately 3900–9100 Å. The exposure times ranged from 2200 to 3600 s with signal-to-noise per resolution element (S/N) between 23 and 35. We visually reviewed each order to remove cosmic rays. Depending on the S/N, we used 10–14 echelle orders within this wavelength range for each spectrum to measure each order's relative radial velocity. We used the spectrum with the highest S/N per resolution element as the reference value for these relative radial velocities.

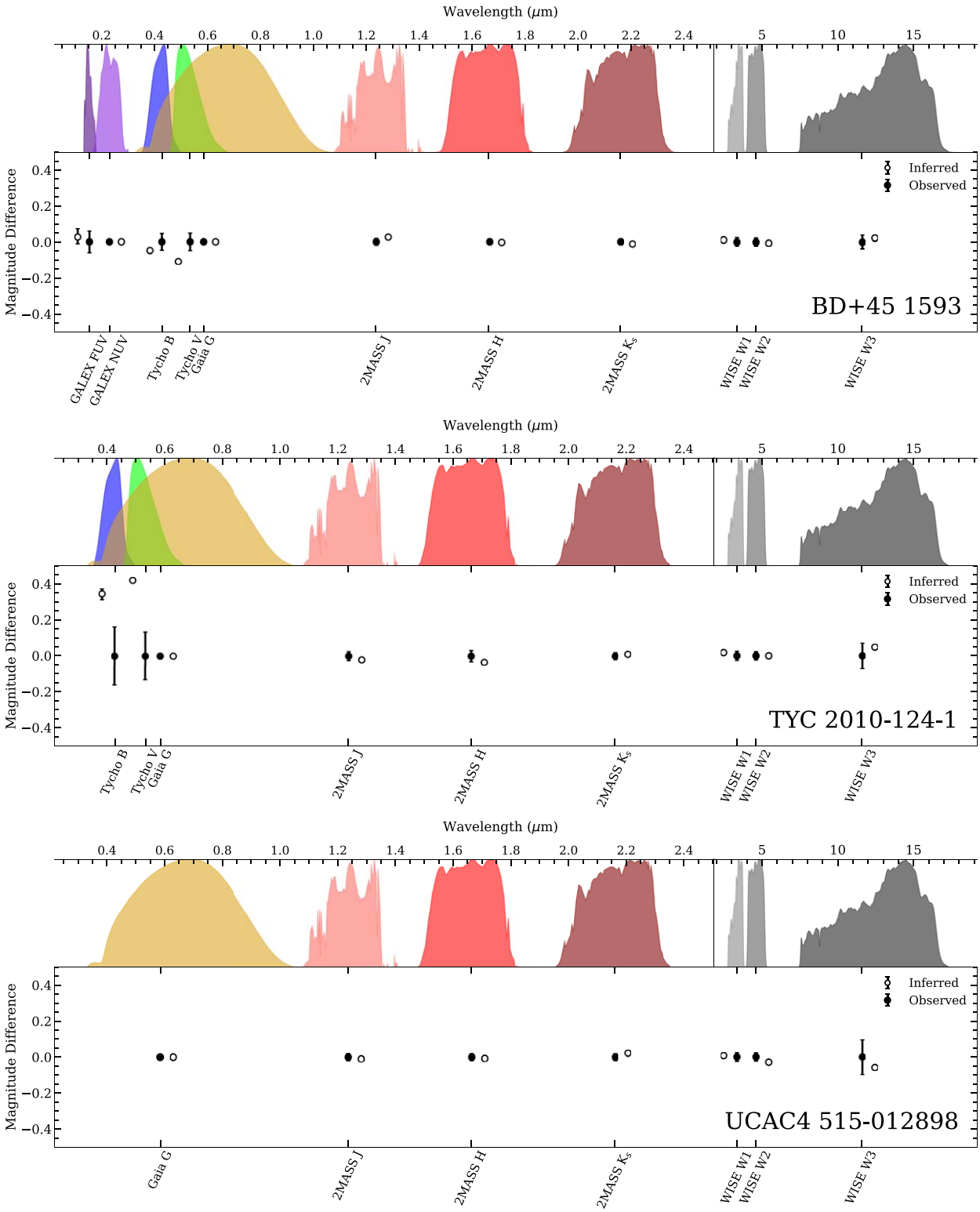

Figure 3. Comparison between the observed magnitudes for the three systems and the isochrone-derived magnitudes of the combined binary system (in the case of BD +45 1593) or the primaries (in the case of TYC 2010-124-1 and UCAC4 515-012898). For each filter, we plot filled circles to represent the observed magnitudes and unfilled circles to represent the isochrone-inferred magnitudes. We plot the relative transmission for each filter obtained from the SVO Filter Profile Service (Rodrigo et al. 2012; Rodrigo & Solano 2020) above its photometric pair. There is a discontinuity on the wavelength axis at the top of each plot between the 2MASS magnitudes and AllWISE magnitudes. The Tycho-2 magnitudes for TYC 2010-124-1 are close to the catalog's limit of reliability (Høg et al. 2000). The B_T magnitude difference corresponds to 2.1σ, which is unsurprising given the number of comparisons in our sample. However, the V_T magnitude difference corresponds to 3.2σ, which we attribute to underestimated random uncertainties or systematic uncertainties at the faint end of the Tycho-2 photometric calibration. The consistency and overall small offsets between the observed and isochrone-inferred magnitudes demonstrate that our method of deriving the host stars' parameters is robust, especially when UV photometry is available.

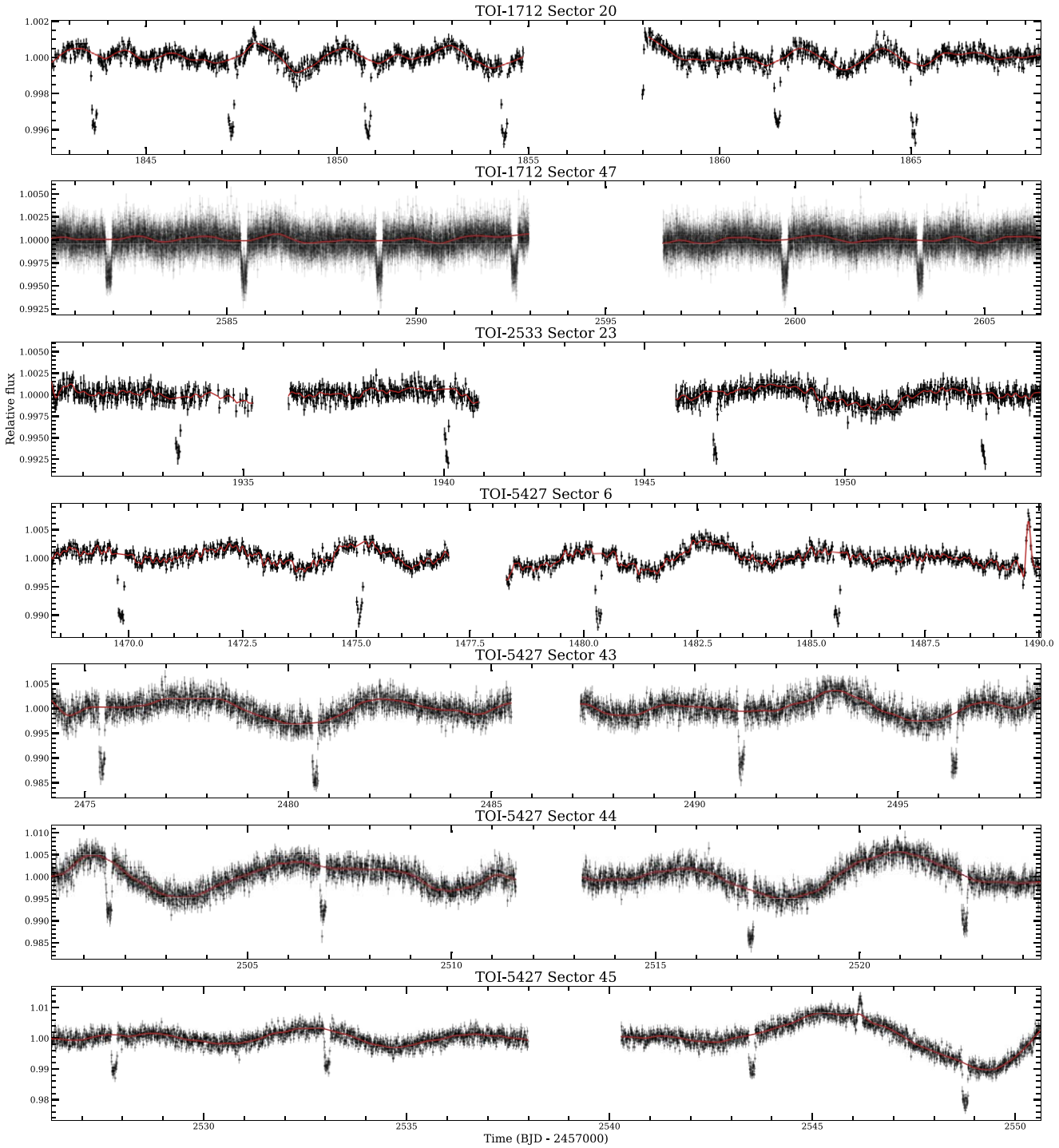

Figure 4. TESS Science Processing Operations Center (SPOC)-reduced light curves for TOI-1712, TOI-2533, and TOI-5427. In addition to the 30 minute cadence data for each of the objects, we include two-minute cadence data for TOI-1712 from TESS Sector 47 and ten-minute cadence data for TOI-5427 from Sectors 43, 44, and 45. We plot in red on top of the data the `juliet`-derived Gaussian process fits the light curves. We next use these fits to detrend the light curves before subsequently fitting the transits.

We also collected three spectra for TOI-1712 between 2020 March 7 and 2023 February 3 using TRES. The exposure times ranged from 600 to 2160 s and with S/N between 35 and 67. These spectra revealed a cross-correlation function indicative of a double-lined spectroscopic binary. The evolution of the cross-correlation function suggests that (1) the primary shows some orbital motion as seen by Gaia and (2) the secondary appears stationary. Combined with the Gaia DR3 SB1 solution, this observation suggests that BD+45 1593 (TOI-1712) is a hierarchical triple system with an unresolved secondary diluting the transit observed by TESS.

We collected 11 spectra of TOI-5427 between 2022 September 25 and 2022 October 7 using the CTIO High Resolution Spectrometer (CHIRON; Tokovinin et al. 2013) high-resolution spectrograph, installed in the 1.5 m telescope at the Cerro Tololo International Observatory. We used an image

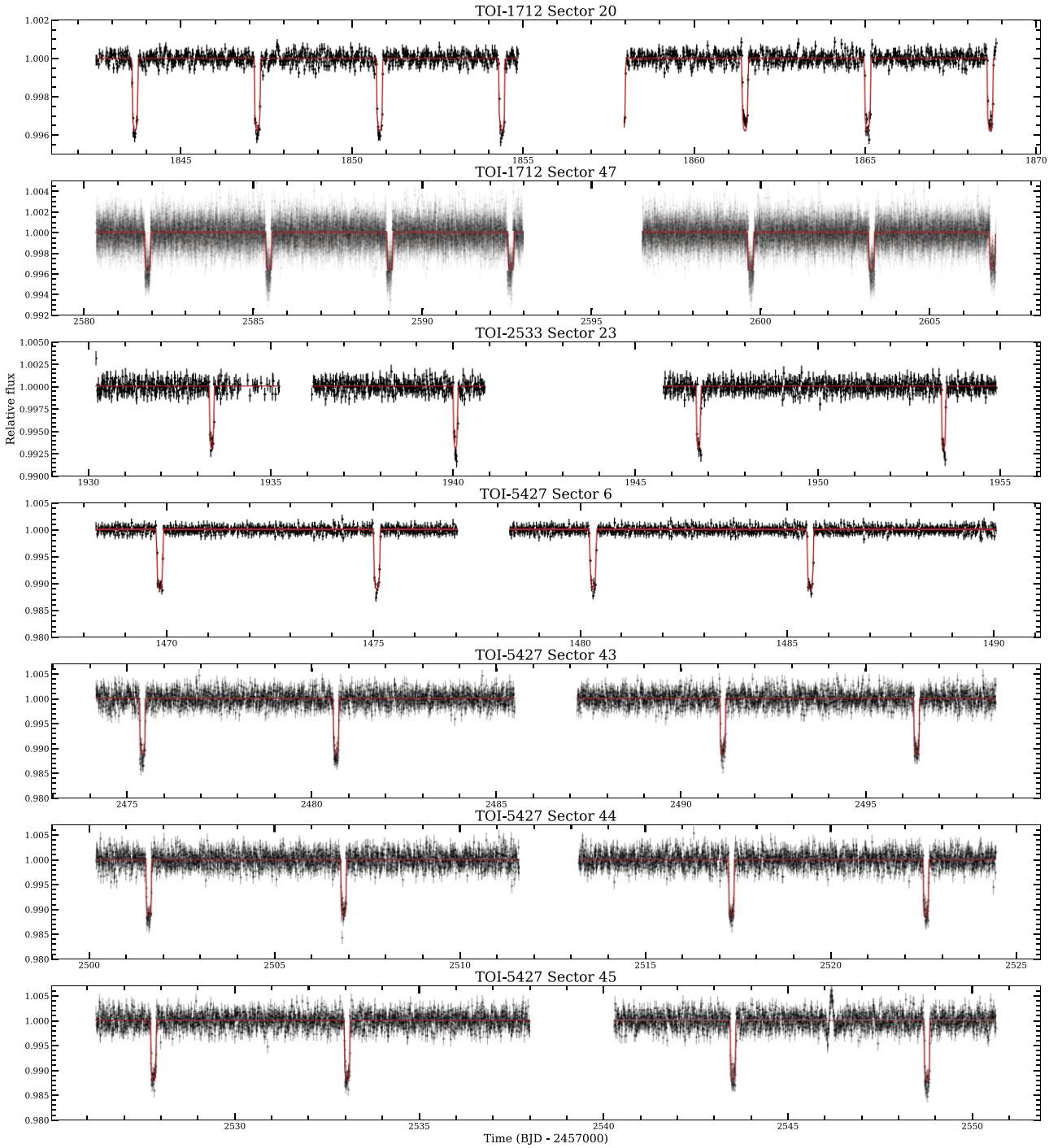

Figure 5. Detrended light curves for TOI-1712, TOI-2533, and TOI-5427. In addition to the 30 minute cadence data for each of the objects, we include two-minute cadence data for TOI-1712 from TESS Sector 47 and ten-minute cadence data for TOI-5427 from Sectors 43, 44, and 45. We overlay the data with red lines representing our `juliet`-derived transit fits. These fits demonstrate that the periods and transit shape parameters reported in the TOI catalog accurately reflect the data and are sufficient for comparison to external catalogs.

slicer that produces spectra with $R \approx 80,000$. The exposure times ranged between 3000 and 3650 s with S/N between 47 and 82 at 550 nm. We calibrated each science spectrum with a thorium-argon (ThAr) spectrum taken immediately beforehand to account for instrumental spectral drift and to compute a new wavelength solution automatically from this calibration with the CHIRON pipeline (Paredes et al. 2021). To extract the radial velocities from these CHIRON observations, we used a least squares deconvolution (Donati et al. 1997) approach where we deconvolved each spectrum against an ATLAS9 synthetic template (Kurucz 1992) following the technique described by Zhou et al. (2020).

We collected five spectra of TOI-5427 between 2022 November 14 and 2023 February 11 using the NEID spectrograph (Halverson et al. 2016; Schwab et al. 2016), a stabilized fiber-fed optical spectrograph on the WIYN 3.5 m telescope at Kitt Peak National Observatory (KPNO). We used the high-resolution (HR) mode that produces spectra with

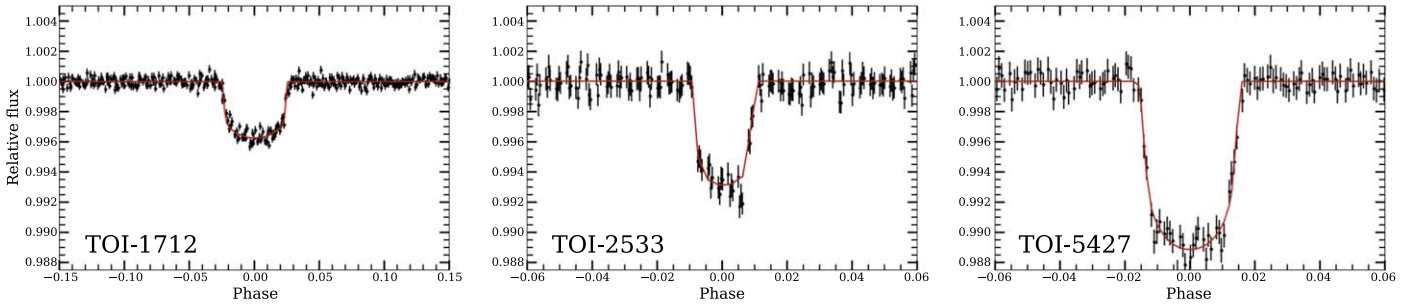

Figure 6. Phased light curves for the 30 minute cadence data of TOI-1712, TOI-2533, and TOI-5427. We overlay the data with red lines representing the `juliet`-derived transit fits. The relative flux axes are consistent across the three objects to illustrate their differing transit depths.

Table 2
Ground-based Radial Velocities

BJD	RV (km s^{-1})	σ_{RV} (km s^{-1})	Source
TOI-5427 (UCAC4 515-012898)			
2459847.882200	−44.961	0.023	CHIRON
2459848.840030	−48.368	0.110	CHIRON
2459849.816380	−38.673	0.033	CHIRON
2459850.875790	−28.476	0.095	CHIRON
2459851.851630	−30.545	0.052	CHIRON
2459852.934530	−42.431	0.038	CHIRON
2459854.774330	−42.442	0.069	CHIRON
2459855.860460	−30.129	0.059	CHIRON
2459856.872970	−28.896	0.036	CHIRON
2459858.810920	−47.816	0.051	CHIRON
2459859.871500	−44.323	0.065	CHIRON
2459899.80424983	−40.6134	0.0167	NEID
2459898.84596773	−30.1702	0.026	NEID
2459897.87815973	−29.9688	0.0304	NEID
2459986.6052418	−32.669	0.0262	NEID
2459983.81974946	−43.1964	0.0277	NEID
TOI-2533 (TYC 2010-124-1)			
2459278.939688	0.00000	0.09313	TRES
2459295.873683	−12.98947	0.06914	TRES
2459296.893338	−8.77543	0.09313	TRES
2459298.965028	−0.02706	0.07976	TRES
2459299.935610	1.81353	0.10406	TRES
2459300.924987	−3.61235	0.14566	TRES
2459301.855739	−12.74344	0.09697	TRES
2459307.836527	−6.70705	0.10400	TRES
2459309.818673	−10.75052	0.07288	TRES
2459311.900542	−1.65152	0.07649	TRES
2459312.931876	1.23157	0.08170	TRES

$R \approx 110,000$ with exposure times of 480 s. The data were reduced using v1.2.0 of the standard NEID Data Reduction Pipeline (NEID-DRP),[18] which derives radial velocities by cross-correlating the observed spectra with a weighted stellar mask (Baranne et al. 1996; Pepe et al. 2002). The median radial velocity precision attained was approximately 26 m s^{-1}.

To fit Keplerian orbits to these ground-based radial velocity data for TOI-2533 and TOI-5427, we use the `thejoker` Python package (Price-Whelan et al. 2017). We do not fit the TRES spectra for TOI-1712. For each system, we use the default priors in `thejoker`: a log-uniform prior in a period set to be between the 1σ confidence interval provided by TESS, a Gaussian prior in Doppler semiamplitude described by $\sigma_K = 1$ km s^{-1}, and a Gaussian prior in systemic velocity described by $\sigma_v = 1$ km s^{-1}. We sample this prior 200,000 times and conduct rejection sampling to obtain a set of initial parameters for use in a `pymc3` (Salvatier et al. 2016) MCMC simulation. Using 10 chains, we generate a posterior distribution of 5000 samples with a burn-in of 20,000 samples. The resulting posterior distributions are both symmetric and unimodal. As suggested by the `thejoker` documentation,[19] this unimodality suggests that these posterior samples are independent and represent a unique solution without the need for convergence tests due to the MCMC sampling method used by `thejoker`. We then take the 16th, 50th, and 84th percentiles of the resulting Doppler semiamplitude and eccentricity posteriors to obtain the values and uncertainties reported in Table 3.

Zero-point offsets between different precision radial velocity spectrographs with amplitudes of a few m s^{-1} are common. We therefore verify that any zero-point offsets have not affected our analysis of TOI-5427. We fit the radial velocities from each instrument with `thejoker` using the same process described above. We then compare the systemic velocity distributions between the two in Figure 7 and obtain the 16th, 50th, and 84th percentiles of the offset distribution by subtracting the systemic velocity posterior from NEID from the systemic velocity posterior from CHIRON. This results in an offset of $-0.6^{+21.0}_{-20.5}$ m s^{-1} that is smaller than the uncertainties of the individual radial velocity measurements. This supports our decision to analyze both data sets without including zero-point offsets between them. We therefore combine the data from CHIRON and NEID to simultaneously fit the ensemble of radial velocities for TOI-5427.

3.3. Determination of the Companions' Properties

We solve the binary star mass function assuming that $\sin^3 i \approx 1$ and re-parameterize Equation (1) as a cubic equation

$$\left(\frac{M_2}{M_1}\right)^3 - B\left(\frac{M_2}{M_1}\right)^2 - 2B\left(\frac{M_2}{M_1}\right) - B = 0, \quad (3)$$

where the coefficient B is defined as

$$B = \frac{1}{2\pi G}\frac{PK_1^3(1-e^2)^{3/2}}{M_1}. \quad (4)$$

Taking the real root of Equation (3) results in a mass ratio that can then be used to determine companion masses given primary masses. Using the inclinations from each system's 30 minute cadence light curve `juliet` transit fit, we find that the $\sin i$ corrections for the companions result in adjustments

[18] https://neid.ipac.caltech.edu/docs/NEID-DRP

[19] https://thejoker.readthedocs.io/en/latest/

Table 3
Properties of the Objects and their Host Stars

Parameter	BD+45 1593	TYC 2010-124-1	UCAC4 515-012898	Source
		Identifiers		
TOI	1712.01	2533.01	5427.01	Guerrero et al. (2021)
TIC	67926921	418012030	52420398	Stassun et al. (2018)
Gaia	917823348536224768	1259922196651254272	3341401062125577088	Gaia DR3
2MASS	J08314698+4449564	J14103331+2625241	J05355241+1255340	2MASS
TYC	2981-1719-1	2010-124-1	⋯	Tycho-2
		Astrometry		
α	127.945701	212.638795	83.968375	Gaia DR3
δ	44.832313	26.423432	12.925942	Gaia DR3
α_{J2000}	$08^h31^m46\overset{s}{.}970745$	$14^h10^m33\overset{s}{.}327483$	$05^h35^m52\overset{s}{.}409305$	Gaia DR3
δ_{J2000}	$44^d49^m56\overset{s}{.}431574$	$26^d25^m24\overset{s}{.}046501$	$12^d55^m33\overset{s}{.}913407$	Gaia DR3
π (mas)	1.7653 ± 0.0182	2.7078 ± 0.0221	2.7589 ± 0.0158	Gaia DR3
		Photometry		
FUV (mag)	18.2406 ± 0.0591	⋯	⋯	GALEX
NUV (mag)	13.9118 ± 0.004	⋯	⋯	GALEX
B_T (mag)	10.817 ± 0.045	12.354 ± 0.16	⋯	Tycho-2
V_T (mag)	10.485 ± 0.047	11.745 ± 0.131	⋯	Tycho-2
G (mag)	10.2738 ± 0.0017	12.0092 ± 0.0018	12.0787 ± 0.0017	Gaia DR2
T (mag)	9.9841 ± 0.0062	11.6417 ± 0.0069	11.659 ± 0.0061	TESS
J (mag)	9.541 ± 0.0182	11.142 ± 0.0242	11.062 ± 0.0201	2MASS
H (mag)	9.374 ± 0.0156	10.872 ± 0.0308	10.753 ± 0.0176	2MASS
K_s (mag)	9.353 ± 0.016	10.8 ± 0.019	10.68 ± 0.0172	2MASS
W1 (mag)	9.314 ± 0.023	10.78 ± 0.024	10.669 ± 0.023	AllWISE
W2 (mag)	9.327 ± 0.021	10.798 ± 0.022	10.701 ± 0.022	AllWISE
W3 (mag)	9.287 ± 0.037	10.735 ± 0.07	10.707 ± 0.096	AllWISE
A_V (mag)	$0.029^{+0.001}_{-0.016}$	$0.019^{+0.001}_{-0.021}$	$0.055^{+0.039}_{-0.039}$	See Footnote
		Spectroscopy		
vbroad (km s^{-1})	30 ± 6	⋯	⋯	Gaia DR3
		Single-lined Spectroscopic Binary Solution		
K_1 (km s^{-1})	7.69 ± 0.61	7.39 ± 1.10	7.86 ± 0.98	Gaia DR3
	⋯	7.575 ± 0.046	9.841 ± 0.018	Ground-Based
e	0.090 ± 0.072	0.195 ± 0.131	0.28 ± 0.11	Gaia DR3
	⋯	0.2473 ± 0.0059	0.0332 ± 0.0015	Ground-Based
P (days)	3.566276 ± 0.0000044	6.6847 ± 0.0034	5.2374183 ± 0.0000056	TESS
		Light Curve Transit Fit		
i (°)	$88.36^{+0.25}_{-0.25}$	$88.01^{+1.34}_{-1.94}$	$87.48^{+1.50}_{-1.65}$	This work
R_2 / R_*	$0.0564^{+0.0006}_{-0.0003}$	$0.079^{+0.004}_{-0.003}$	$0.097^{+0.002}_{-0.002}$	This work
		Physical Properties		
$T_{\rm eff}$ (K)	6860^{+40}_{-30}	6180^{+60}_{-60}	6160^{+70}_{-40}	This Work
log g	$3.67^{+0.03}_{-0.02}$	$4.36^{+0.03}_{-0.03}$	$4.34^{+0.03}_{-0.02}$	This Work
[Fe/H]	$-0.2^{+0.1}_{-0.1}$	$-0.3^{+0.2}_{-0.2}$	$-0.2^{+0.1}_{-0.1}$	This Work
$M_\star$ ($M_\odot$)	$1.63^{+0.01}_{-0.02}$	$1.02^{+0.06}_{-0.07}$	$1.07^{+0.06}_{-0.05}$	This Work
$R_\star$ ($R_\odot$)	$3.10^{+0.07}_{-0.10}$	$1.11^{+0.01}_{-0.01}$	$1.16^{+0.01}_{-0.01}$	This Work
Age (Gyr)	$1.62^{+0.05}_{-0.03}$	$4.26^{+2.18}_{-1.74}$	$3.96^{+1.24}_{-1.53}$	This Work
M_2 ($M_{\rm Jup}$)	82^{+7}_{-7} (*)	72^{+3}_{-3}	93^{+3}_{-3}	This Work
R_2 ($R_{\rm Jup}$)	$1.74^{+0.08}_{-0.07}$	$0.85^{+0.04}_{-0.03}$	$1.15^{+0.03}_{-0.03}$	This Work

Note. We derive the secondary mass for TYC 2010-124-1 and UCAC4 515-012898 using ground-based radial velocity data from TRES and both CHIRON and NEID, respectively. We use Lallement et al. (2022) and Vergely et al. (2022) for the A_V extinctions.

smaller than 0.1%. The inclination uncertainties are therefore insignificant in comparison to our mass estimate uncertainties.

We use the 30 minute cadence light curve `juliet`-inferred radius ratio posteriors to calculate the secondary radii R_2 in Jupiter radii. In the TOI-1712 system, the flux from the eclipsing pair is diluted by an unresolved secondary revealed by the TRES spectra. We correct the dilution in the TOI-1712 light curve by incorporating into a `juliet` transit fit the TESS T-band flux ratio from our `isochrones` binary star fit posterior. We first take each point in the `isochrones` posterior and calculate the flux ratio of the secondary to the primary

$$F = \frac{f_{\rm B}}{f_{\rm Aa}} = 10^{(T_{\rm Aa} - T_{\rm B})/2.5}, \quad (5)$$

where $T_{\rm Aa}$ and $T_{\rm B}$ are the TESS T-band magnitudes of the primary and secondary. We next calculate the dilution D in the light curve for each point

$$D = \frac{1}{1 + F}. \quad (6)$$

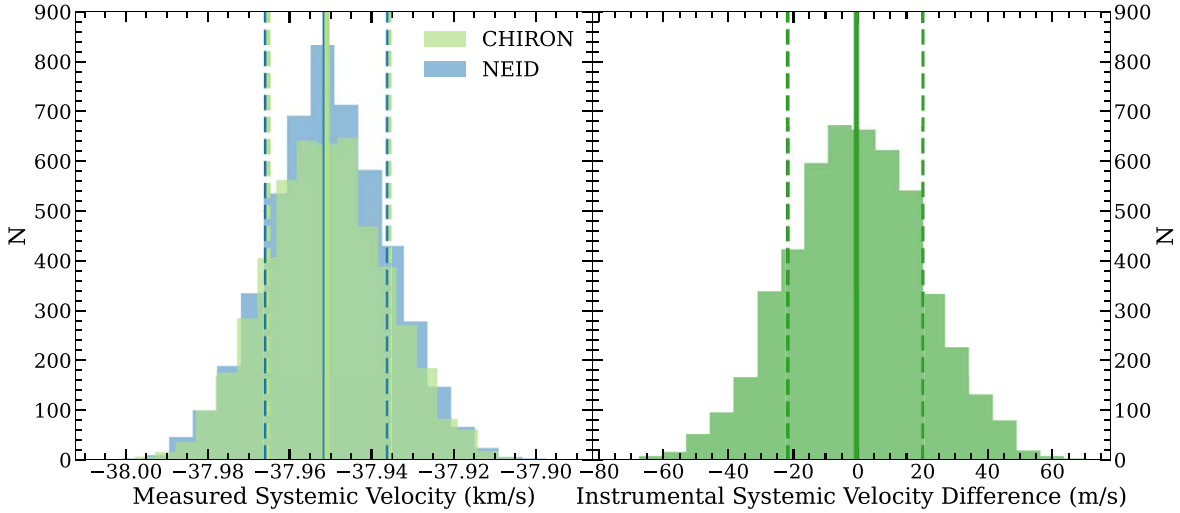

Figure 7. Comparison between CHIRON and NEID velocity zero-point offsets for TOI-5427. We plot distribution medians as solid vertical lines and the 16th and 84th percentiles as dashed vertical lines. Left: Distributions of Monte Carlo samples from `thejoker` Doppler solution systemic velocities after fitting to radial velocity measurements taken by CHIRON and NEID. Right: Distribution of the differences between the two distributions in the left-hand panel. The resulting median offset is much smaller than the individual radial velocity uncertainties, suggesting that the data sets are consistent with each other.

We then fit the 30 minute cadence light curve of TOI-1712 for each point using the same procedure described in Section 3.1, but with the dilution prior set to be the posterior point's calculated dilution. We obtain the median radius ratio from each point's individual `juliet` posterior and use these points as our full radius ratio posterior for BD+45 1593. We then use the same procedure as with TYC 2010-124-1 and UCAC4 515-012898 to obtain the companion radius for BD+45 1593.

We use a Monte Carlo simulation to infer the mass and radius uncertainties for these three systems. We generate normal distributions for each `thejoker` Doppler analysis-derived (for TYC 2010-124-1 and UCAC4 515-012898) or Gaia/TESS-derived (for BD+45 1593) parameter. The number of Monte Carlo trials is equal to the lesser of the number of data points in the mass and radius posterior distributions from `isochrones` and the number of data points in the radius ratio posterior from `juliet` (about 3000 samples). For the posterior with more data points, we randomly select a number of posterior points equal to the number of data points in the smaller posterior without replacement. For each set of points in the combined posteriors, we calculate a mass and radius inference for the companion, resulting in distributions that we characterize with their 16th, 50th, and 84th percentiles reported in Table 3. This approach captures the covariance between the stellar parameters from the isochrone fit in order to generate an accurate uncertainty for the companion mass and radius inferences. A caveat is that our reported uncertainties only include random uncertainties. The inclusion of systematic uncertainties would likely result in larger overall uncertainties (e.g., Tayar et al. 2022).

We account for contamination in the TESS light curve for UCAC4 515-012898 (TOI-5427), where the TESS contamination ratio is 26.3055%. This level of light curve contamination corresponds to a radius underestimate of 5.13%, so we increase our inferred radius for UCAC4 515-012898 b (TOI-5427) by 5.13% to account for this effect. BD+45 1593 (TOI-1712) and TYC 2010-124-1 (TOI-2533) have TESS contamination ratios indicative of radii underestimates that are smaller than our report uncertainties, so we do not increase uncertainties in either case. We provide corner plots illustrating this process and visualizing the covariances for each system in Figure 8.

4. Discussion

Our synthesis of Gaia DR3 SB1 solutions and TESS transit discoveries described in this article has revealed a new transiting brown dwarf and two very-low-mass eclipsing binary companions. We confirm that TOI-2533.01 is a $72^{+3}_{-3}\,M_{\rm Jup} = 0.069^{+0.003}_{-0.003}\,M_{\odot}$ transiting brown dwarf, placing it in a class of only a few dozen such objects. We include in Table 4 an up-to-date list of known transiting brown dwarfs. We further confirm that TOI-5427.01 with a mass of $93^{+3}_{-3}\,M_{\rm Jup} = 0.088^{+0.002}_{-0.002}\,M_{\odot}$ is one of the lowest-mass stars that models suggest is just above the hydrogen-burning limit for its composition. We validate TOI-1712.01 as an inflated $82^{+7}_{-7}\,M_{\rm Jup} = 0.079^{+0.007}_{-0.007}\,M_{\odot}$ very-low-mass star in a hierarchical triple system.

The Gaia DR3 SB1 solutions for brown dwarfs and very-low-mass stars are consistent with the ground-based precision radial velocity-based SB1 solutions. While the Gaia Doppler semiamplitude for TYC 2010-124-1 is in good agreement with ground-based follow-up observations, it appears that Gaia has underestimated by about 2 km s^{-1} the Doppler semiamplitude of UCAC4 515-012898. The Gaia DR3 SB1 solutions also suggest a higher eccentricity for UCAC4 515-012898 and a slight phase shift for TYC 2010-124-1. We are unable to further investigate this issue, as the individual Gaia radial velocity measurements are not publicly available. For these two systems, the agreement between the Gaia DR3 and ground-based precision radial velocity SB1 solutions suggests that Gaia DR3 SB1 solutions are sufficiently precise to characterize massive brown dwarfs and low-mass stars.

It seems possible that the quality of the Gaia DR3 SB1 solution is proportional to the number of "good" radial velocity observations available by the time of Gaia DR3. The brown dwarf TYC 2010-124-1 b has 47 "good" Gaia DR3 radial velocities, while the very-low-mass stars BD+45 1593 Ab and UCAC4 515-012898 b only have 18 and 25, respectively. We suggest that the number of "good" Gaia radial velocities may be a useful metric for assessing future Gaia SB1 solutions. The

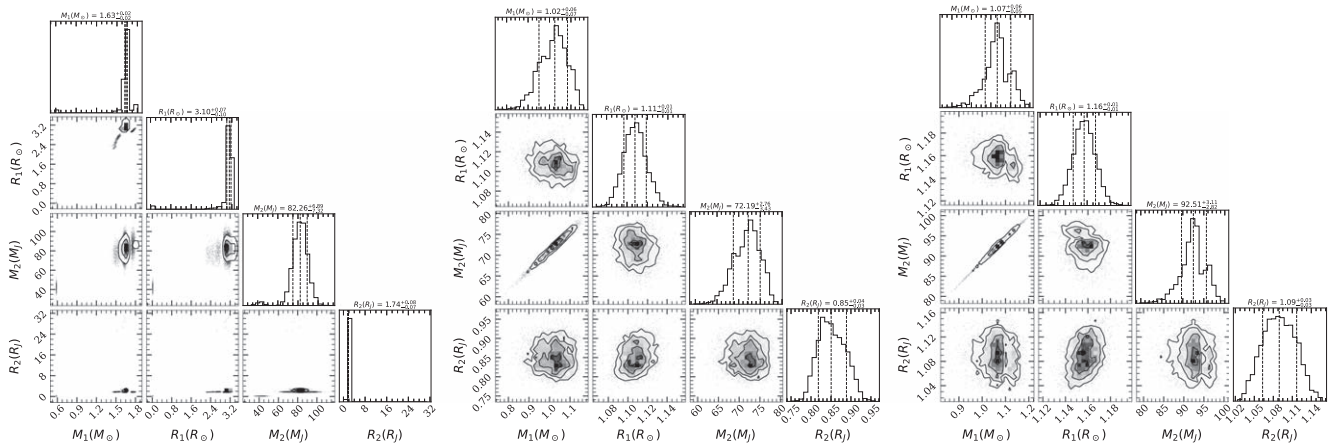

Figure 8. Corner plots showing unimodal posteriors for BD+45 1593 (left), TYC 2010-124-1 (center), and UCAC4 515-012898 (right).

fact that BD+45 1593 is an SB2 system may have affected Gaia's SB1 fit to its radial velocity variations. BD+45 1593 A is both hot and rotating quickly, and all of these facts make it a challenging target for Doppler observations.

We plot our inferred masses and radii for the three secondaries in Figure 9. While we find that our mass and radius inferences for TYC 2010-124-1 b are consistent with the Chabrier et al. (2023) theoretical models for brown dwarfs, the radius of UCAC4 515-012898 b is about 6% larger than predicted by the Baraffe et al. (2015) theoretical models for isolated stars of the same mass, as is often the case for low-mass stars. In contrast, the radius of BD+45 1593 Ab $R_2 = 1.74^{+0.08}_{-0.07}\,R_{\rm Jup}$, is more than 80% larger than the radius $R \approx 1.0\,R_{\rm Jup}$ predicted by the Baraffe et al. (2015) models for an isolated star with similar mass, composition, and age. Because the MIST and PAdova TRieste Stellar Evolutionary Code (PARSEC; Bressan et al. 2012; Nguyen et al. 2022) isochrone grids do not extend to these objects' mass ranges, we are unable to use them for comparison. Given the precisions of our mass, age, composition, and radius inferences, we find at over 9σ significance that BD+45 1593 Ab is inflated. We note that this estimate accounts for dilution from BD+45 1593 B, and in any case, dilution typically would lead to an underestimated radius.

Observations of radii about 10% larger than predicted by theoretical models appear to be ubiquitous among K and M dwarfs (Kraus et al. 2011; Birkby et al. 2012). These larger observed radii correspond to observed temperatures typically 5% cooler than predicted by models, though this effect is poorly studied due to the difficulty of determining late-type stellar temperatures (Ribas et al. 2008; Morales et al. 2009; Torres 2013). Magnetic fields are the most-favored explanation for this "radius inflation problem" (and its parallel "temperature suppression problem"), as they can increase the radii of stars yet are rarely included in stellar models. Strong magnetic fields are responsible for the significant starspot coverage of late-type dwarfs and may inhibit convective energy transport (Feiden & Chaboyer 2013). The net result of these two physical mechanisms is an increase in the photospheric radii of K and M dwarfs.

To empirically correct for radius underestimates, attempts have been made in the past to relate magnetic activity with proxies like rotation (Somers & Stassun 2017; Jaehnig et al. 2019), X-ray emission (López-Morales 2007), and Hα emission (Stassun et al. 2012). On the other hand, Mann et al. (2015) found no correlation between radius discrepancy and either Hα or X-ray emission. While models have had some success including magnetic fields in the context of X-ray emission (MacDonald & Mullan 2014), the magnetic field strengths required in this context might not be realistic (Feiden & Chaboyer 2014). More quantitative predictions from Browning et al. (2016) provided an upper bound for the possible strength of these magnetic fields via magnetohydrodynamic simulations, and MacDonald & Mullan (2015) provided a constraint based on lithium abundance. While this remains an active area of research, it appears that magnetic fields contribute to radius inflation in low-mass stars without accounting for all aspects of the radius inflation problem.

The eventual solution of the radius inference problem is important, as accurate and precise radii for low-mass stars are required for the inference of accurate and precise radii for the apparently common planets transiting low-mass stars (Cassan et al. 2012). As low-mass stars are also the most common type of star in the galaxy (Bochanski et al. 2010), we expect that a sizable portion of the Milky Way's exoplanet population orbits low-mass stars. Because of their small separations and high transit probabilities, habitable zone terrestrial planets are easier to find orbiting low-mass stars than solar-type stars. Low-mass stars are therefore the preferred target for habitable transiting planet search programs (Gould et al. 2003) like MEarth (Nutzman & Charbonneau 2008), the TRAnsiting Planets and PlanetesImals Small Telescope (TRAPPIST; Jehin et al. 2011), the Next-Generation Transit Survey (NGTS; West et al. 2016), and TESS (Ricker et al. 2014). Unaccounted for, the radius inflation problem would lead to underestimated radii for planets transiting M dwarfs. An underestimated radius could cause a nonterrestrial, uninhabitable planet to be mistakenly classified as a terrestrial, possibly habitable planet.

We propose that the intense instellation experienced by BD +45 1593 Ab is primarily responsible for its inflated radius. It has been suggested that in binary systems with two very-low-mass stars, instellation-driven radius inflation is limited to 5% (Lucy 2017). In this situation though, BD+45 1593 Ab is experiencing 500 times more flux than in the situation investigated by Lucy (2017). The increased surface temperature resulting from this instellation could decrease the temperature gradient of BD+45 1593 Ab near its surface, thereby limiting the ability of convection to transport energy in the same manner as magnetic fields. This diminished efficiency of convective energy transport would then lead to the inflated radius of

Table 4
Literature Sample of Transiting Brown Dwarfs as of June 2023

Name	Simbad Name	P (days)	M_{BD} (M_{Jup})	R_{BD} (R_{Jup})	Eccentricity	M_* ($M_\odot$)	R_* ($R_\odot$)	T_{eff} (K)	[Fe/H]	Reference
TYC 2010-124-1 b	TYC 2010-124-1	$6.6847^{+0.0034}_{-0.0034}$	72^{+3}_{-3}	$0.85^{+0.04}_{-0.03}$	$0.2473^{+0.0059}_{-0.0059}$	$1.02^{+0.06}_{-0.07}$	$1.11^{+0.01}_{-0.01}$	6180^{+60}_{-60}	$-0.3^{+0.2}_{-0.2}$	This Work
TOI-2119 b	StM 274	7.201	$64.4^{+2.3}_{-2.2}$	$1.08^{+0.03}_{-0.03}$	$0.337^{+0.0019}_{-0.00064}$	$0.525^{+0.02}_{-0.021}$	$0.5^{+0.015}_{-0.015}$	3621^{+48}_{-46}	$0.055^{+0.084}_{-0.077}$	1
TOI-2521 b	TYC 5362-881-1	5.563	$77.5^{+3.3}_{-3.3}$	$1.01^{+0.04}_{-0.04}$	<0.035	$1.1^{+0.07}_{-0.07}$	$1.77^{+0.068}_{-0.068}$	5600^{+100}_{-100}	$-0.3^{+0.3}_{-0.3}$	2
TOI-2336 b	TYC 7317-698-1	7.712	$69.9^{+2.3}_{-2.3}$	$1.05^{+0.04}_{-0.04}$	$0.01^{+0.006}_{-0.005}$	$1.41^{+0.08}_{-0.08}$	$1.781^{+0.059}_{-0.059}$	6550^{+100}_{-100}	$0^{+0.3}_{-0.3}$	2
TOI-2543 b	TYC 229-654-1	7.543	$67.62^{+3.45}_{-3.45}$	$0.95^{+0.09}_{-0.09}$	$0.009^{+0.003}_{-0.002}$	$1.29^{+0.08}_{-0.08}$	$1.86^{+0.15}_{-0.15}$	6060^{+82}_{-82}	$-0.28^{+0.1}_{-0.1}$	3
TOI-1982 b	BD-22 3669	17.172	$65.85^{+2.75}_{-2.72}$	$1.08^{+0.04}_{-0.04}$	$0.272^{+0.014}_{-0.014}$	$1.41^{+0.08}_{-0.08}$	$1.51^{+0.05}_{-0.05}$	6325^{+110}_{-110}	$-0.1^{+0.09}_{-0.09}$	3
TOI-629 b	HD 44717	8.718	$66.98^{+2.96}_{-2.95}$	$1.11^{+0.05}_{-0.05}$	$0.298^{+0.008}_{-0.008}$	$2.16^{+0.13}_{-0.13}$	$2.37^{+0.11}_{-0.11}$	9100^{+200}_{-200}	$0.1^{+0.15}_{-0.15}$	3
TOI-1994 b	HD 298656	4.03	22	1.28	0.29	…	…	7550	…	4
GPX-1 b	UCAC4 731-024744	1.75	$19.7^{+1.6}_{-1.6}$	$1.47^{+0.10}_{-0.10}$	…	$1.68^{+0.10}_{-0.10}$	$1.56^{+0.10}_{-0.10}$	7000^{+200}_{-200}	…	5
TOI-746 b	TOI-746	10.98	$82.2^{+4.9}_{-4.4}$	$0.95^{+0.09}_{-0.06}$	$0.199^{+0.003}_{-0.003}$	$0.98^{+0.06}_{-0.06}$	$0.957^{+0.051}_{-0.051}$	5593^{+215}_{-215}	$0.01^{+0.29}_{-0.29}$	6
TOI-587 b	HD 74162	8.04	$81.1^{+7.1}_{-7.0}$	$1.32^{+0.07}_{-0.06}$	$0.051^{+0.049}_{-0.036}$	$2.32^{+0.14}_{-0.14}$	$2.031^{+0.092}_{-0.092}$	10400^{+300}_{-300}	$0.07^{+0.12}_{-0.12}$	6
TOI-148 b	TOI-148	4.87	$77.1^{+5.8}_{-4.6}$	$0.81^{+0.05}_{-0.06}$	$0.005^{+0.006}_{-0.004}$	$1.03^{+0.06}_{-0.06}$	$1.192^{+0.068}_{-0.068}$	5836^{+286}_{-286}	$-0.28^{+0.28}_{-0.28}$	6
NGTS-19 b	NGTS-19	17.8397	$69.5^{+5.7}_{-5.4}$	$1.034^{+0.055}_{-0.053}$	$0.3767^{+0.0061}_{-0.0061}$	$0.807^{+0.038}_{-0.043}$	$0.896^{+0.04}_{-0.035}$	4716^{+39}_{-28}	$0.11^{+0.074}_{-0.07}$	7
TOI-1278 B	TOI-1278	14.476	$18.5^{+0.5}_{-0.5}$	$1.09^{+0.24}_{-0.2}$	$0.013^{+0.004}_{-0.004}$	$0.55^{+0.02}_{-0.02}$	$0.573^{+0.012}_{-0.012}$	3799^{+42}_{-42}	$-0.01^{+0.28}_{-0.28}$	8
TOI-811 b	TOI-811	25.166	$59^{+13}_{-8.6}$	$1.26^{+0.06}_{-0.06}$	$0.509^{+0.075}_{-0.075}$	$1.32^{+0.07}_{-0.07}$	$1.27^{+0.09}_{-0.09}$	6107^{+77}_{-77}	$0.4^{+0.09}_{-0.09}$	9
TOI-852 b	TOI-852	4.946	$53.7^{+1.4}_{-1.4}$	$0.83^{+0.04}_{-0.04}$	$0.004^{+0.004}_{-0.004}$	$1.32^{+0.05}_{-0.05}$	$1.72^{+0.04}_{-0.04}$	5768^{+84}_{-84}	$0.33^{+0.09}_{-0.09}$	9
HATS-70 b	HATS-70	1.888	$12.9^{+1.8}_{-1.8}$	$1.38^{+0.08}_{-0.08}$	<0.18	$1.78^{+0.12}_{-0.12}$	$1.88^{+0.07}_{-0.07}$	7930^{+820}_{-820}	$0.04^{+0.11}_{-0.11}$	10
KELT-1 b	KELT-1	1.218	$27.4^{+0.9}_{-0.9}$	$1.12^{+0.04}_{-0.04}$	$0.01^{+0.01}_{-0.01}$	$1.34^{+0.06}_{-0.06}$	$1.47^{+0.05}_{-0.05}$	6516^{+49}_{-49}	$0.05^{+0.08}_{-0.08}$	11
NLTT 41135 b	LP 563-38	2.889	$33.7^{+2.8}_{-2.8}$	$1.13^{+0.27}_{-0.27}$	<0.02	$0.19^{+0.03}_{-0.03}$	$0.21^{+0.02}_{-0.02}$	3230^{+130}_{-130}	$-0.25^{+0.25}_{-0.25}$	12
LHS 6343c	G 205-57	12.713	$62.9^{+2.3}_{-2.3}$	$0.83^{+0.02}_{-0.02}$	$0.056^{+0.032}_{-0.032}$	$0.37^{+0.01}_{-0.01}$	$0.38^{+0.01}_{-0.01}$	…	$0.02^{+0.19}_{-0.19}$	13
LP 261-75 b	LP 261-75	1.882	$68.1^{+2.1}_{-2.1}$	$0.9^{+0.02}_{-0.02}$	<0.007	$0.3^{+0.02}_{-0.02}$	$0.31^{+0.01}_{-0.01}$	3100^{+50}_{-50}	…	14
WASP-30 b	WASP-30	4.157	$62.5^{+1.2}_{-1.2}$	$0.95^{+0.03}_{-0.03}$	0 (adopted)	$1.25^{+0.04}_{-0.04}$	$1.4^{+0.03}_{-0.03}$	6202^{+51}_{-51}	$0.08^{+0.1}_{-0.1}$	15
WASP-128 b	WASP-128	2.209	$37.2^{+0.9}_{-0.9}$	$0.94^{+0.02}_{-0.02}$	<0.007	$1.16^{+0.04}_{-0.04}$	$1.15^{+0.02}_{-0.02}$	5950^{+50}_{-50}	$0.01^{+0.12}_{-0.12}$	16
CoRoT-3 b	CoRoT-3	4.257	21.7^{+1}_{-1}	$1.01^{+0.07}_{-0.07}$	0 (adopted)	$1.37^{+0.09}_{-0.09}$	$1.56^{+0.09}_{-0.09}$	6740^{+140}_{-140}	$-0.02^{+0.06}_{-0.06}$	17
CoRoT-15 b	CoRoT-15	3.06	$63.3^{+4.1}_{-4.1}$	$1.12^{+0.3}_{-0.3}$	0 (adopted)	$1.32^{+0.12}_{-0.12}$	$1.46^{+0.31}_{-0.31}$	6350^{+200}_{-200}	$0.1^{+0.2}_{-0.2}$	18
CoRoT-33 b	CoRoT-33	5.819	$59^{+1.8}_{-1.8}$	$1.1^{+0.53}_{-0.53}$	$0.07^{+0.002}_{-0.002}$	$0.86^{+0.04}_{-0.04}$	$0.94^{+0.14}_{-0.14}$	5225^{+80}_{-80}	$0.44^{+0.1}_{-0.1}$	19
Kepler-39 b	Kepler-39	21.087	$20.1^{+1.3}_{-1.3}$	$1.24^{+0.1}_{-0.1}$	$0.112^{+0.057}_{-0.057}$	$1.29^{+0.07}_{-0.07}$	$1.4^{+0.1}_{-0.1}$	6350^{+100}_{-100}	$0.1^{+0.14}_{-0.14}$	20
KOI-189 b	Kepler-486	30.36	$78^{+3.4}_{-3.4}$	$1^{+0.02}_{-0.02}$	$0.275^{+0.004}_{-0.004}$	$0.76^{+0.05}_{-0.05}$	$0.73^{+0.02}_{-0.02}$	4952^{+40}_{-40}	$-0.07^{+0.12}_{-0.12}$	21
KOI-205 b	Kepler-492	11.72	39.9^{+1}_{-1}	$0.81^{+0.02}_{-0.02}$	<0.031	$0.92^{+0.03}_{-0.03}$	$0.84^{+0.02}_{-0.02}$	5237^{+60}_{-60}	$0.14^{+0.12}_{-0.12}$	22
KOI-415 b	KOI-415	166.788	$62.1^{+2.7}_{-2.7}$	$0.79^{+0.12}_{-0.12}$	$0.689^{+0.001}_{-0.001}$	$0.94^{+0.06}_{-0.06}$	$1.15^{+0.15}_{-0.15}$	5810^{+80}_{-80}	$-0.24^{+0.11}_{-0.11}$	23
EPIC 201702477 b	UCAC2 33047398	40.737	$66.9^{+1.7}_{-1.7}$	$0.76^{+0.07}_{-0.07}$	$0.228^{+0.003}_{-0.003}$	$0.87^{+0.03}_{-0.03}$	$0.9^{+0.06}_{-0.06}$	5517^{+70}_{-70}	$-0.16^{+0.05}_{-0.05}$	24
EPIC 212036875 b	TYC 1400-1873-1	5.17	$52.3^{+1.9}_{-1.9}$	$0.87^{+0.02}_{-0.02}$	$0.132^{+0.004}_{-0.004}$	$1.29^{+0.07}_{-0.07}$	$1.5^{+0.03}_{-0.03}$	6238^{+60}_{-60}	$0.01^{+0.1}_{-0.1}$	25
AD 3116 b	Cl* NGC 2632 HSHJ 430	1.983	$54.2^{+4.3}_{-4.3}$	$1.02^{+0.28}_{-0.28}$	$0.146^{+0.024}_{-0.024}$	$0.28^{+0.02}_{-0.02}$	$0.29^{+0.08}_{-0.08}$	3200^{+200}_{-200}	$0.16^{+0.1}_{-0.1}$	26
CWW 89 Ab	UCAC4 366-166973	5.293	$36.84^{+0.97}_{-0.97}$	$0.94^{+0.03}_{-0.03}$	$0.1929^{+0.002}_{-0.002}$	$1.01^{+0.04}_{-0.04}$	$1.01^{+0.03}_{-0.03}$	5850^{+85}_{-85}	$0.03^{+0.08}_{-0.08}$	27
RIK 72 b	UGCS J160339.22-185129.4	97.76	$59.2^{+6.8}_{-6.8}$	$3.1^{+0.31}_{-0.31}$	$0.146^{+0.012}_{-0.012}$	$0.44^{+0.04}_{-0.04}$	$0.96^{+0.1}_{-0.1}$	3349^{+142}_{-142}	…	28
TOI-503 b	BD+13 1880	3.677	$53.7^{+1.2}_{-1.2}$	$1.34^{+0.26}_{-0.15}$	0 (adopted)	$1.8^{+0.06}_{-0.06}$	$1.7^{+0.05}_{-0.05}$	7650^{+160}_{-160}	$0.61^{+0.07}_{-0.07}$	29
TOI-569 b	CD-41 3255	6.556	63.8^{+1}_{-1}	$0.75^{+0.02}_{-0.02}$	<0.0035	$1.21^{+0.03}_{-0.03}$	$1.48^{+0.03}_{-0.03}$	5705^{+76}_{-76}	$0.4^{+0.08}_{-0.08}$	30
TOI-1406 b	HD 274870	10.574	$46^{+2.7}_{-2.7}$	$0.86^{+0.02}_{-0.02}$	<0.039	$1.18^{+0.09}_{-0.09}$	$1.35^{+0.03}_{-0.03}$	6290^{+100}_{-100}	$-0.08^{+0.09}_{-0.09}$	30
NGTS-7 Ab	NGTS-7	0.676	$75.5^{+3}_{-13.7}$	$1.38^{+0.13}_{-0.14}$	0 (adopted)	$0.48^{+0.13}_{-0.13}$	$0.61^{+0.06}_{-0.06}$	3359^{+106}_{-106}	…	31
2M0535-05 a	V* V2384 Ori	9.779	$56.7^{+4.8}_{-4.8}$	$6.5^{+0.33}_{-0.33}$	$0.323^{+0.006}_{-0.006}$	…	…	…	…	32
2M0535-05 b	V* V2384 Ori	9.779	$35.6^{+2.8}_{-2.8}$	$5.00^{+0.25}_{-0.25}$	$0.323^{+0.006}_{-0.006}$	…	…	…	…	32
2M1510 Aa	2MASS J15104786-2818174	20.902	$40^{+2.9}_{-2.9}$	$1.53^{+0.15}_{-0.15}$	$0.309^{+0.022}_{-0.022}$	…	…	…	…	33

Table 4
(Continued)

Name	Simbad Name	P (days)	$M_{\rm BD}$ ($M_{\rm Jup}$)	$R_{\rm BD}$ ($R_{\rm Jup}$)	Eccentricity	M_* ($M_\odot$)	R_* ($R_\odot$)	$T_{\rm eff}$ (K)	[Fe/H]	Reference
2M1510 Ab	2MASS J15104761-2818234	20.902	$39.9^{+2.9}_{-2.9}$	$1.53^{+0.15}_{-0.15}$	$0.309^{+0.022}_{-0.022}$	...	...	...	...	33
CoRoT-34 b	UCAC4 431-022970	2.119	$71.4^{+8.9}_{-8.6}$	$1.09^{+0.17}_{-0.16}$	0 (adopted)	$1.66^{+0.08}_{-0.15}$	$1.85^{+0.29}_{-0.25}$	7820^{+160}_{-160}	$-0.2^{+0.2}_{-0.2}$	34
Kepler-503 b	Kepler-503	7.258	$78.6^{+3.1}_{-3.1}$	$0.96^{+0.06}_{-0.04}$	$0.025^{+0.014}_{-0.012}$	$1.154^{+0.047}_{-0.042}$	$1.764^{+0.08}_{-0.068}$	5670^{+100}_{-110}	$0.169^{+0.046}_{-0.045}$	35
HIP 33609 b	HD 52470	39.472	$68.0^{+7.4}_{-7.4}$	$1.580^{+0.074}_{-0.070}$	$0.560^{+0.029}_{-0.031}$	$2.383^{+0.10}_{-0.095}$	$1.863^{+0.087}_{-0.082}$	10400^{+800}_{-600}	$-0.01^{+0.19}_{-0.20}$	36
TOI-2336 b	TYC 7317-698-1	7.71	$69.9^{+2.3}_{-2.3}$	$1.05^{+0.04}_{-0.04}$	$0.010^{+0.006}_{-0.005}$	$1.40^{+0.07}_{-0.07}$	$1.82^{+0.06}_{-0.06}$	6433^{+84}_{-84}	$0.09^{+0.11}_{-0.11}$	37

Note.1: Carmichael et al. (2022), Cañas et al. (2022); 2: Lin et al. (2023); 3: Psaridi et al. (2022); 4: Page et al. (2023); 5: Benni et al. (2021); 6: Grieves et al. (2021); 7: Acton et al. (2021); 8: Artigau (2021); 9: Carmichael et al. (2021); 10: Zhou et al. (2019); 11: Siverd et al. (2012); 12: Irwin et al. (2010); 13: Johnson et al. (2011); 14: Irwin et al. (2018); 15: Triaud et al. (2013); 16: Hodžić et al. (2018); 17: Deleuil et al. (2008); 18: Bouchy et al. (2011a); 19: Csizmadia et al. (2015); 20: Bouchy et al. (2011b); 21: Díaz et al. (2014); 22: Díaz et al. (2013); 23: Moutou et al. (2013); 24: Bayliss et al. (2017); 25: Carmichael et al. (2019); 26: Gillen et al. (2017); 27: Nowak et al. (2017); 28: David et al. (2019); 29: Šubjak (2020); 30: Carmichael et al. (2020); 31: Jackman et al. (2019); 32: Stassun et al. (2006); 33: Triaud et al. (2020); 34: Sebastian et al. (2022); 35: Cañas et al. (2018); 36: Vowell et al. (2023); 37: Lin et al. (2023).

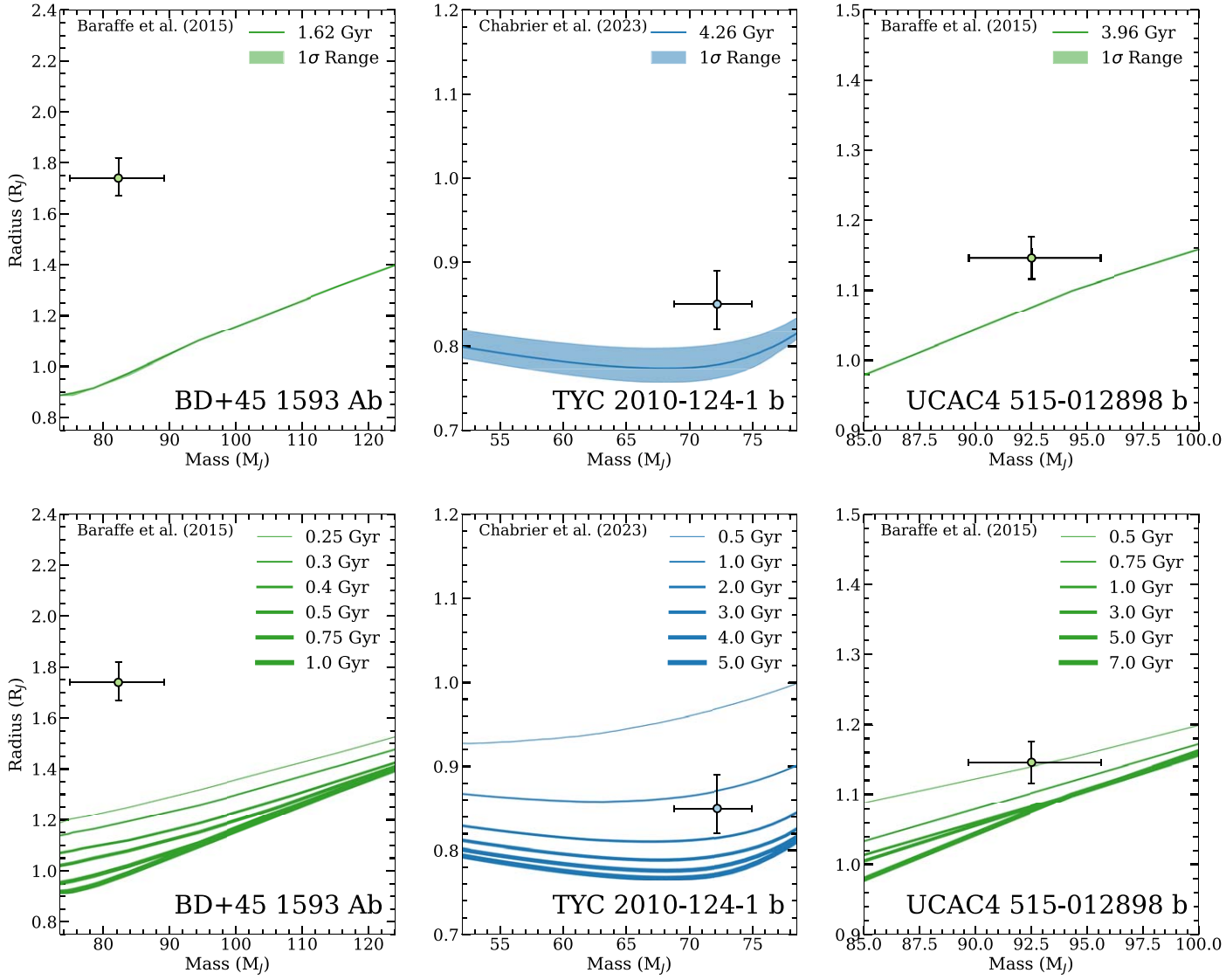

Figure 9. Comparisons between predicted and observed masses and radii. Top: mass–radius relations assuming our isochrone-inferred system ages. We plot the mass–radius relation at each system's age as the solid line and indicate its 1σ uncertainty as the shaded region. Bottom: mass–radius relations assuming a range of ages. Thicker lines refer to older ages. BD+45 1593 Ab has a significantly larger radius than predicted by the Baraffe et al. (2015) theoretical models. UCAC4 515-012898 b is slightly bigger than predicted by the Baraffe et al. (2015) theoretical models as is frequently observed for low-mass stars. TYC 2010-124-1 b is consistent with the Chabrier et al. (2023) models. The models we use assume solar metallicity, while our systems have slightly subsolar metallicities. However, these differences in metallicity are too small to produce a radius offset as large as we observe for BD+45 1593 Ab. Indeed, at the low-mass end of the MIST isochroe grid at $M_* \approx 0.11\ M_\odot \approx 110\ M_{\rm Jup}$ a 0.2 dex decrease in [Fe/H] corresponds to no more than a 5% decrease in stellar radius.

BD+45 1593 Ab. Indeed, the photospheric temperature of an isolated star with similar properties to BD+45 1593 Ab is expected to be $T_{\rm eff} \approx 2300$ (Baraffe et al. 2015). Given its instellation, the "day side" equilibrium temperature of BD+45 1593 Ab could be as high as $T_{\rm eq} \approx 4400$ K assuming a Bond albedo $A_{\rm B} = 0$ and no redistribution of heat.

Tidal effects may also play a role in the inflated radius of BD +45 1593 Ab, perhaps in a process analogous to the shear mixing that may occur in massive binaries (Song et al. 2013). The fully convective nature of BD+45 1593 Ab would make shear mixing inefficient, and its small eccentricity likely minimizes the importance of tidal dissipation for its inflated radius. The probable fast rotation of BD+45 1593 Ab resulting from its circular orbit, short circularization time, and therefore likely spin–orbit synchronization could contribute to its inflated radius, though the relationship between rotation and radius inflation is unclear (Jackson et al. 2019). Consequently, we conclude that instellation is the best candidate to explain the inflated radius of BD+45 1593 Ab.

We searched the light curves of TOI-1712 and TOI-5427 for secondary eclipses perfectly opposite the transits of TOI-1712.01 and TOI-5427.01 as expected for circular orbits. We were unable to identify a secondary eclipse in either case. This is not surprising, as the detection of a secondary eclipse would have eliminated these objects from consideration for inclusion in the TOI catalog. Given the precision of the TESS data for TOI-1712 and TOI-5427 and the expected secondary eclipse durations of TOI-1712.01 and TOI-5427.01, we would have been able to identify secondary eclipses above 0.003% for TOI-1712 and above 0.01% for TOI-5427. This lack of a secondary eclipse detection does not constrain the "day side" temperature for UCAC4 515-012898 b, as we expect its photospheric temperature to have been undetectable given our limits. On the other hand, the nondetection of a secondary eclipse for TOI-

1712.01 limits the "day side" temperature of BD+45 1593 Ab to less than 3200 K. The "day side" of BD+45 1593 Ab could be as hot as 4400 K if its albedo is zero and heat is not redistributed, so our nondetection of a secondary eclipse implies that either its albedo is nonzero or the redistribution of heat is efficient.

We compare TYC 2010-124-1 b to the Chabrier et al. (2023) brown dwarf isochrones in Figure 9. Isolated brown dwarfs cool and contract to settle into a typical mass range of between 0.7 and 1.4 Jupiter radii (Deleuil et al. 2008; Šubjak 2020; Carmichael et al. 2020) after at least 100 Myr. Objects younger than this tend to be larger Stassun et al. 2006; David et al. 2019. According to isolated brown dwarf evolution models (e.g., Baraffe et al. 2003; Saumon & Marley 2008; Phillips et al. 2020; Marley et al. 2021; Carmichael 2023), the rate of this contraction should decrease over time. However, the details of this process are unclear (Carmichael 2023). We find that the radius of TYC 2010-124-1 b is 9% bigger than the model prediction for an isolated brown dwarf, but this offset is only significant at the 1.9σ level.

The radius inflation we observe in BD+45 1593 Ab potentially parallels the processes responsible for the inflation of some hot Jupiters (e.g., Grunblatt et al. 2016, 2017, 2022b; Wittenmyer et al. 2022). Hot Jupiters orbiting evolved stars are sometimes observed with larger radii than hot Jupiters orbiting main sequence stars (Grunblatt et al. 2019). In this case, the inflated radii of mature hot Jupiters orbiting evolved stars have been "reinflated" due to the rapid transport of energy deposited into their surface layers by their evolved host star into their interiors (e.g., Lopez & Fortney 2016; Thorngren & Fortney 2018; Thorngren et al. 2021). Intense instellation may therefore be capable of inflating radii from the giant planet regime up to the very-low-mass star regime.

Because theoretical models have struggled to explain the data that is currently available, a much larger sample of massive brown dwarfs and very-low-mass stars with precisely inferred radii relative to their solar-type primaries could lead to useful empirical radius calibrations. Our approach that combines Gaia SB1 solutions with transit discoveries from Kepler, K2, TESS, and the future PLAnetary Transits and Oscillations (PLATO) mission has the potential to precisely characterize over 400 brown dwarfs and low-mass stars. Such a catalog of radii precisely inferred relative to the radii of their primaries could be the basis of future empirical brown dwarf and low-mass star mass–radius relations. The masses inferred in this way using the Doppler technique with a known inclination are more precise and likely more accurate than other currently employed methods of mass inference such as astrometry or atmospheric fitting.[20] As transit surveys typically focus on low-mass stars to find small-radius planets, these empirical stellar radii could lead to better planet radii which would lead to better atmospheric and interior structure inferences for terrestrial planets like those in the TRAPPIST-1 system.

5. Conclusion

We characterized three transiting systems: one brown dwarf and two low-mass stars in the TYC 2010-124-1, UCAC4 515-012898, and BD+45 1593 systems identified by TESS as TOI-2533.01, TOI-5427.01, and TOI-1712.01. We showed that the synthesis of Gaia DR3 SB1 solutions and TESS TOI discoveries offers a promising path to the large-scale, homogeneous characterization of low-mass stars and massive brown dwarfs. Gaia DR3 SB1 solutions and TESS transits indicated that the masses of the transiting objects in all three systems were consistent with the brown dwarf-mass range. Ground-based precision radial velocity measurements confirmed that TOI-2533.01 is a transiting brown dwarf with $M = 72^{+3}_{-3}\,M_{\rm Jup} = 0.069^{+0.003}_{-0.003}\,M_{\odot}$ and that TOI-5427.01 is a transiting very-low-mass star with $M = 93^{+2}_{-2}\,M_{\rm Jup} = 0.088^{+0.002}_{-0.002}\,M_{\odot}$. We validated TOI-1712.01 as a very-low-mass star with $M = 82^{+7}_{-7}\,M_{\rm Jup} = 0.079^{+0.007}_{-0.007}\,M_{\odot}$ transiting a massive subgiant primary in the hierarchical triple system BD+45 1593. The star BD+45 1593 Ab has a radius nearly 80% larger than predicted by theoretical models for an isolated star with similar masses, solar composition, and age equal to that of the primary BD+45 1593 Aa. While the observation of very-low-mass stars with radii larger than predicted by theoretical models seems to be ubiquitous and often attributed to magnetic fields, radius inflation as large as we observe in BD+45 1593 Ab cannot be attributed to the effect of magnetic fields alone. We suggest that the intense instellation experienced by BD+45 1593 Ab heats its photosphere beyond the photospheric temperature expected for an isolated star with similar parameters. This increased photospheric temperature diminishes the temperature gradient in the outer parts of BD+45 1593 Ab, suppresses convection, and leads to its inflated radius. Future studies of systems with Gaia SB1 solutions and Kepler, K2, TESS, or PLATO transit detections have the potential to provide hundreds of precise radius inferences for brown dwarfs and very-low-mass stars. These latter data would be critical for the calibration of empirical mass–radius relations for very-low-mass stars that would be very useful for the calculation of the radii of planets transiting very-low-mass stars like those in the TRAPPIST-1 system.

Acknowledgments

We thank the anonymous referee for many very helpful comments. We thank Zafar Rustamkulov for helpful suggestions about visualizing our results. We also thank Daniel Thorngren for his helpful insight into our findings. This material is based upon work supported by the National Science Foundation under grant No. 2009415 and by the TESS General Investigator program under NASA grant 80NSSC20K0059. S. N.Q. acknowledges support from the TESS mission via subaward s3449 from MIT. This work was supported by a NASA WIYN PI Data Award, administered by the NASA Exoplanet Science Institute. This work has made use of data from the European Space Agency (ESA) mission Gaia (https://www.cosmos.esa.int/gaia), processed by the Gaia Data Processing and Analysis Consortium (DPAC; https://www.cosmos.esa.int/web/gaia/dpac/consortium). Funding for the DPAC has been provided by national institutions, in particular, the institutions participating in the Gaia Multilateral Agreement. This paper includes data collected with the TESS mission, obtained from the MAST data archive at the Space Telescope Science Institute (STScI). Funding for the TESS mission is provided by the NASA Explorer Program. STScI is operated by the Association of Universities for Research in Astronomy, Inc., under NASA contract NAS 526555. We acknowledge the use of public TESS data from pipelines at the TESS Science Office and at the TESS Science Processing

[20] Different mass inference methods have yielded inconsistent mass results for the first confirmed brown dwarf Gliese 229 B (Marley et al. 1996; Brandt et al. 2020).

Operations Center. This research has made use of the Exoplanet Follow-up Observation Program (ExoFOP; DOI:10.26134/ExoFOP5) website, which is operated by the California Institute of Technology, under contract with the National Aeronautics and Space Administration under the Exoplanet Exploration Program. Resources supporting this work were provided by the NASA High-End Computing (HEC) Program through the NASA Advanced Supercomputing (NAS) Division at Ames Research Center for the production of the SPOC data products. This paper contains data taken with the NEID instrument, which was funded by the NASA-NSF Exoplanet Observational Research (NN-EXPLORE) partnership and built by Pennsylvania State University. NEID is installed on the WIYN telescope, which is operated by the National Optical Astronomy Observatory, and the NEID archive is operated by the NASA Exoplanet Science Institute at the California Institute of Technology. NN-EXPLORE is managed by the Jet Propulsion Laboratory, California Institute of Technology under contract with the National Aeronautics and Space Administration. Data presented herein were obtained at the WIYN Observatory from telescope time allocated to NN-EXPLORE through the scientific partnership of the National Aeronautics and Space Administration, the National Science Foundation, and NOIRLab. The authors are honored to be permitted to conduct astronomical research on Iolkam Duag (Kitt Peak), a mountain with particular significance to the Tohono O'odham. This publication makes use of data products from 2MASS, which is a joint project of the University of Massachusetts and the Infrared Processing and Analysis Center/California Institute of Technology, funded by the National Aeronautics and Space Administration and the National Science Foundation. This publication makes use of data products from the Wide-field Infrared Survey Explorer, which is a joint project of the University of California, Los Angeles, and the Jet Propulsion Laboratory/California Institute of Technology, and NEOWISE, which is a project of the Jet Propulsion Laboratory/California Institute of Technology. WISE and NEOWISE are funded by the National Aeronautics and Space Administration. Some/all of the data presented in this paper were obtained from the Mikulski Archive for Space Telescopes (MAST). STScI is operated by the Association of Universities for Research in Astronomy, Inc., under NASA contract NAS5-26555. Support for MAST for non–Hubble Space Telescope data is provided by the NASA Office of Space Science via grant NNX13AC07G and by other grants and contracts. This research has made use of the Exoplanet Follow-up Observation Program website, which is operated by the California Institute of Technology, under contract with the National Aeronautics and Space Administration under the Exoplanet Exploration Program. This research has made use of the Spanish Virtual Observatory (https://svo.cab.inta-csic.es) project funded by MCIN/AEI/10.13039/501100011033/ through grant PID2020-112949GB-I00. This research has made use of the SIMBAD database (Wenger et al. 2000), operated at CDS, Strasbourg, France. This research made use of Lightkurve, a Python package for Kepler and TESS data analysis (Collaboration et al. 1812). This work made use of the IPython package (Perez & Granger 2007). This research has made use of NASA's Astrophysics Data System.

Facilities: ADS, CDS, CTIO:1.5m (CHIRON), CTIO:2-MASS, ExoFOP, FLWO:1.5m (TRES), FLWO:2MASS, Gaia, GALEX, IRSA, MAST, NEOWISE, TESS, WISE, WIYN (NEID).

Software: astropy (Astropy Collaboration et al. 2013, 2018, 2022), `isochrones` (Morton 2015), `juliet` (Espinoza et al. 2019), matplotlib (Hunter 2007), numpy (Harris et al. 2020), pandas (pandas development team, T 2020; Wes McKinney 2010), PyMultiNest (Buchner et al. 2014), `R` (R Core Team 2023), scipy (Jones et al. 2011; Virtanen et al. 2020), `thejoker` (Price-Whelan et al. 2017).

ORCID iDs

Stephen P. Schmidt https://orcid.org/0000-0001-8510-7365
Kevin C. Schlaufman https://orcid.org/0000-0001-5761-6779
Keyi Ding (丁可怿) https://orcid.org/0000-0001-8470-1725
Samuel K. Grunblatt https://orcid.org/0000-0003-4976-9980
Theron Carmichael https://orcid.org/0000-0001-6416-1274
Allyson Bieryla https://orcid.org/0000-0001-6637-5401
Joseph E. Rodriguez https://orcid.org/0000-0001-8812-0565
Jack Schulte https://orcid.org/0000-0002-7382-0160
Noah Vowell https://orcid.org/0000-0002-0701-4005
George Zhou https://orcid.org/0000-0002-4891-3517
Samuel N. Quinn https://orcid.org/0000-0002-8964-8377
Samuel W. Yee https://orcid.org/0000-0001-7961-3907
Joshua N. Winn https://orcid.org/0000-0002-4265-047X
Joel D. Hartman https://orcid.org/0000-0001-8732-6166
David W. Latham https://orcid.org/0000-0001-9911-7388
Douglas A. Caldwell https://orcid.org/0000-0003-1963-9616
M. M. Fausnaugh https://orcid.org/0000-0002-9113-7162
Christina Hedges https://orcid.org/0000-0002-3385-8391
Jon M. Jenkins https://orcid.org/0000-0002-4715-9460
Hugh P. Osborn https://orcid.org/0000-0002-4047-4724
S. Seager https://orcid.org/0000-0002-6892-6948

References

Acton, J. S., Goad, M. R., Burleigh, M. R., et al. 2021, MNRAS, 505, 2741
Arenou, F., Luri, X., Babusiaux, C., et al. 2018, A&A, 616, A17
Astropy Collaboration, Price-Whelan, A. M., Lim, P. L., et al. 2022, ApJ, 935, 167
Astropy Collaboration, Price-Whelan, A. M., Sipőcz, B. M., et al. 2018, AJ, 156, 123
Astropy Collaboration, Robitaille, T. P., Tollerud, E. J., et al. 2013, A&A, 558, A33
Artigau, É., Hébrard, G., Cadieux, C., et al. 2021, AJ, 162, 144
Babusiaux, C., Fabricius, C., Khanna, S., et al. 2023, A&A, 674, A32
Bailer-Jones, C. A. L., Rybizki, J., Fouesneau, M., Demleitner, M., & Andrae, R. 2021, AJ, 161, 147
Baraffe, I., Chabrier, G., Barman, T. S., Allard, F., & Hauschildt, P. H. 2003, A&A, 402, 701
Baraffe, I., Homeier, D., Allard, F., & Chabrier, G. 2015, A&A, 577, A42
Baranne, A., Queloz, D., Mayor, M., et al. 1996, A&AS, 119, 373
Bayliss, D., Hojjatpanah, S., Santerne, A., et al. 2017, AJ, 153, 15
Benni, P., Burdanov, A. Y., Krushinsky, V. V., et al. 2021, MNRAS, 505, 4956
Bianchi, L., Shiao, B., & Thilker, D. 2017, ApJS, 230, 24
Birkby, J., Nefs, B., Hodgkin, S., et al. 2012, MNRAS, 426, 1507
Bochanski, J. J., Hawley, S. L., Covey, K. R., et al. 2010, AJ, 139, 2679
Bouchy, F., Deleuil, M., Guillot, T., et al. 2011a, A&A, 525, A68
Bouchy, F., Bonomo, A. S., Santerne, A., et al. 2011b, A&A, 533, A83
Brandt, T. D., Dupuy, T. J., Bowler, B. P., et al. 2020, AJ, 160, 196
Bressan, A., Marigo, P., Girardi, L., et al. 2012, MNRAS, 427, 127

Browning, M. K., Weber, M. A., Chabrier, G., & Massey, A. P. 2016, ApJ, 818, 189
Buchner, J., Georgakakis, A., Nandra, K., et al. 2014, A&A, 564, A125
Caldwell, D. A., Tenenbaum, P., Twicken, J. D., et al. 2020, RNAAS, 4, 201
Cañas, C. I., Bender, C. F., Mahadevan, S., et al. 2018, ApJL, 861, L4
Cañas, C. I., Mahadevan, S., Bender, C. F., et al. 2022, AJ, 163, 89
Carmichael, T. W. 2023, MNRAS, 519, 5177
Carmichael, T. W., Irwin, J. M., Murgas, F., et al. 2022, MNRAS, 514, 4944
Carmichael, T. W., Latham, D. W., & Vanderburg, A. M. 2019, AJ, 158, 38
Carmichael, T. W., Quinn, S. N., Mustill, A. J., et al. 2020, AJ, 160, 53
Carmichael, T. W., Quinn, S. N., Zhou, G., et al. 2021, AJ, 161, 97
Cassan, A., Kubas, D., Beaulieu, J.-P., et al. 2012, Natur, 481, 167
Chabrier, G., Baraffe, I., Phillips, M., & Debras, F. 2023, A&A, 671, A119
Choi, J., Dotter, A., Conroy, C., et al. 2016, ApJ, 823, 102
Collaboration, Lightkurve, Cardoso, & Hedges, J. V. d. M. 1812, Lightkurve: Kepler and TESS time series analysis in Python, Astrophysics Source Code Library, ascl:1812.013
Creevey, O. L., Sordo, R., Pailler, F., et al. 2023, A&A, 674, A26
Csizmadia, S., Hatzes, A., Gandolfi, D., et al. 2015, A&A, 584, A13
David, T. J., Hillenbrand, L. A., Gillen, E., et al. 2019, ApJ, 872, 161
Deleuil, M., Deeg, H. J., Alonso, R., et al. 2008, A&A, 491, 889
Díaz, R. F., Damiani, C., Deleuil, M., et al. 2013, A&A, 551, L9
Díaz, R. F., Montagnier, G., Leconte, J., et al. 2014, A&A, 572, A109
Donati, J.-F., Semel, M., Carter, B. D., Rees, D. E., & Collier Cameron, A. 1997, MNRAS, 291, 658
Dotter, A. 2016, ApJS, 222, 8
Espinoza, N., Kossakowski, D., & Brahm, R. 2019, MNRAS, 490, 2262
Evans, D. W., Riello, M., De Angeli, F., et al. 2018, A&A, 616, A4
Fabricius, C., Luri, X., Arenou, F., et al. 2021, A&A, 649, A5
Feiden, G. A., & Chaboyer, B. 2013, ApJ, 779, 183
Feiden, G. A., & Chaboyer, B. 2014, ApJ, 789, 53
Feroz, F., & Hobson, M. P. 2008, MNRAS, 384, 449
Feroz, F., Hobson, M. P., & Bridges, M. 2009, MNRAS, 398, 1601
Feroz, F., Hobson, M. P., Cameron, E., & Pettitt, A. N. 2019, OJAp, 2, 10
Fűrész, G. 2008, PhD thesis, University of Szeged, Hungary
Fouesneau, M., Frémat, Y., Andrae, R., et al. 2023, A&A, 674, A28
Gaia Collaboration, Brown, A. G. A., Vallenari, A., et al. 2018, A&A, 616, A1
Gaia Collaboration, Brown, A. G. A., Vallenari, A., et al. 2021, A&A, 649, A1
Gaia Collaboration, Prusti, T., de Bruijne, J. H. J., et al. 2016, A&A, 595, A1
Gaia Collaboration, Vallenari, A., Brown, A. G. A., et al. 2023a, A&A, 674, A1
Gaia Collaboration, Arenou, F., Babusiaux, C., et al. 2023b, A&A, 674, A34
Gillen, E., Hillenbrand, L. A., David, T. J., et al. 2017, ApJ, 849, 11
Gould, A., Pepper, J., & DePoy, D. L. 2003, ApJ, 594, 533
Grieves, N., Bouchy, F., Lendl, M., et al. 2021, A&A, 652, A127
Grunblatt, S. K., Huber, D., Gaidos, E., et al. 2017, AJ, 154, 254
Grunblatt, S. K., Huber, D., Gaidos, E., et al. 2019, AJ, 158, 227
Grunblatt, S. K., Huber, D., Gaidos, E. J., et al. 2016, AJ, 152, 185
Grunblatt, S. K., Saunders, N., Sun, M., et al. 2022a, AJ, 163, 120
Grunblatt, S. K., Saunders, N., Sun, M., et al. 2022b, AJ, 163, 120
Guerrero, N. M., Seager, S., Huang, C. X., et al. 2021, ApJS, 254, 39
Halverson, S., Terrien, R., Mahadevan, S., et al. 2016, Proc. SPIE, 9908, 99086P
Harris, C. R., Millman, K. J., van der Walt, S. J., et al. 2020, Natur, 585, 357
Hodžić, V., Triaud, A. H. M. J., Anderson, D. R., et al. 2018, MNRAS, 481, 5091
Høg, E., Fabricius, C., Makarov, V. V., et al. 2000, A&A, 355, L27
Huang, C. X., Vanderburg, A., Pál, A., et al. 2020a, RNAAS, 4, 204
Huang, C. X., Vanderburg, A., Pál, A., et al. 2020b, RNAAS, 4, 206
Hunter, J. D. 2007, CSE, 9, 90
Irwin, J., Buchhave, L., Berta, Z. K., et al. 2010, ApJ, 718, 1353
Irwin, J. M., Charbonneau, D., Esquerdo, G. A., et al. 2018, AJ, 156, 140
Jackman, J. A. G., Wheatley, P. J., Bayliss, D., et al. 2019, MNRAS, 489, 5146
Jackson, R. J., Jeffries, R. D., Deliyannis, C. P., Sun, Q., & Douglas, S. T. 2019, MNRAS, 483, 1125
Jaehnig, K., Somers, G., & Stassun, K. G. 2019, ApJ, 879, 39
Jehin, E., Gillon, M., Queloz, D., et al. 2011, Msngr, 145, 2
Jenkins, J. M., Twicken, J. D., McCauliff, S., et al. 2016, Proc. SPIE, 99133E
Jermyn, A. S., Bauer, E. B., Schwab, J., et al. 2023, ApJS, 265, 15
Johnson, J. A., Apps, K., Gazak, J. Z., et al. 2011, ApJ, 730, 79
Jones, E., Oliphant, T., Peterson, P., et al. 2011, SciPy: Open source scientific tools for Python, http://www.scipy.org/
Katz, D., Sartoretti, P., Guerrier, A., et al. 2023, A&A, 674, A5
Kipping, D. M. 2013, MNRAS, 435, 2152
Kovács, G., Zucker, S., & Mazeh, T. 2002, A&A, 391, 369
Kraus, A. L., Tucker, R. A., Thompson, M. I., Craine, E. R., & Hillenbrand, L. A. 2011, ApJ, 728, 48
Kunimoto, M., Daylan, T., Guerrero, N., et al. 2022, ApJS, 259, 33
Kurucz, R. L. 1992, in IAU Symp. 149, The Stellar Populations of Galaxies, ed. B. Barbuy & A. Renzini (Dordrecht: Kluwer), 225
Lallement, R., Vergely, J. L., Babusiaux, C., & Cox, N. L. J. 2022, A&A, 661, A147
Lin, Z., Gan, T., Wang, S. X., et al. 2023, MNRAS, 523, 6162
Lindegren, L., Bastian, U., Biermann, M., et al. 2021a, A&A, 649, A4
Lindegren, L., Klioner, S. A., Hernández, J., et al. 2021b, A&A, 649, A2
Lopez, E. D., & Fortney, J. J. 2016, ApJ, 818, 4
López-Morales, M. 2007, ApJ, 660, 732
Lucy, L. B. 2017, A&A, 601, A75
MacDonald, J., & Mullan, D. J. 2014, ApJ, 787, 70
MacDonald, J., & Mullan, D. J. 2015, MNRAS, 448, 2019
Mainzer, A., Bauer, J., Grav, T., et al. 2011, ApJ, 731, 53
Mann, A. W., Feiden, G. A., Gaidos, E., Boyajian, T., & von Braun, K. 2015, ApJ, 804, 64
Marley, M. S., Saumon, D., Guillot, T., et al. 1996, Sci, 272, 1919
Marley, M. S., Saumon, D., Visscher, C., et al. 2021, ApJ, 920, 85
Morales, J. C., Ribas, I., Jordi, C., et al. 2009, ApJ, 691, 1400
Morton, T. D., 2015 isochrones: Stellar model grid package, Astrophysics Source Code Library, ascl:1503.010
Moutou, C., Bonomo, A. S., Bruno, G., et al. 2013, A&A, 558, L6
Nguyen, C. T., Costa, G., Girardi, L., et al. 2022, A&A, 665, A126
Nowak, G., Palle, E., Gandolfi, D., et al. 2017, AJ, 153, 131
Nutzman, P., & Charbonneau, D. 2008, PASP, 120, 317
Page, E., Pepper, J., Wright, D., et al. 2023, arXiv:2305.08836
pandas development team, T 2020, pandas-dev/pandas: Pandas, v.1.5.0, Zenodo, 10.5281/zenodo.3509134
Paredes, L. A., Henry, T. J., Quinn, S. N., et al. 2021, AJ, 162, 176
Paxton, B., Bildsten, L., Dotter, A., et al. 2011, ApJS, 192, 3
Paxton, B., Cantiello, M., Arras, P., et al. 2013, ApJS, 208, 4
Paxton, B., Schwab, J., Bauer, E. B., et al. 2018, ApJS, 234, 34
Paxton, B., Smolec, R., Schwab, J., et al. 2019, ApJS, 243, 10
Pecaut, M. J., & Mamajek, E. E. 2013, ApJS, 208, 9
Pepe, F., Mayor, M., Galland, F., et al. 2002, A&A, 388, 632
Perez, F., & Granger, B. E. 2007, CSE, 9, 21
Phillips, M. W., Tremblin, P., Baraffe, I., et al. 2020, A&A, 637, A38
Pourbaix, D., Arenou, F., Gavras, P., et al. 2022, Gaia Data Release 3 Documentation release 1.3, https://gea.esac.esa.int/archive/documentation/GDR3/index.html
Pourbaix, D., Tokovinin, A. A., Batten, A. H., et al. 2004, A&A, 424, 727
Price-Whelan, A. M., Hogg, D. W., Foreman-Mackey, D., & Rix, H.-W. 2017, ApJ, 837, 20
Prša, A., Kochoska, A., Conroy, K. E., et al. 2022, ApJS, 258, 16
Psaridi, A., Bouchy, F., Lendl, M., et al. 2022, A&A, 664, A94
R Core Team 2023, The R Project for Statistical Computing, https://www.R-project.org/
Ribas, I., Morales, J. C., Jordi, C., et al. 2008, MmSAI, 79, 562
Ricker, G. R., Winn, J. N., Vanderspek, R., et al. 2014, Proc. SPIE, 9143, 20
Riello, M., De Angeli, F., Evans, D. W., et al. 2018, A&A, 616, A3
Rodrigo, C., & Solano, E. 2020, in Contributions to the XIV.0 Scientific Meeting (virtual) of the Spanish Astronomical Society (La Laguna: SEA), 182
Rodrigo, C., Solano, E., & Bayo, A. 2012, SVO Filter Profile Service Version 1.0, IVOA
Rowell, N., Davidson, M., Lindegren, L., et al. 2021, A&A, 649, A11
Salvatier, J., Wieckiâ, T. V., & Fonnesbeck, C., 2016 PyMC3: Python probabilistic programming framework, Astrophysics Source Code Library, ascl:1610.016
Saumon, D., & Marley, M. S. 2008, ApJ, 689, 1327
Saunders, N., Grunblatt, S. K., Huber, D., et al. 2022, AJ, 163, 53
Schwab, C., Rakich, A., Gong, Q., et al. 2016, Proc. SPIE, 9908, 99087H
Sebastian, D., Guenther, E. W., Deleuil, M., et al. 2022, MNRAS, 516, 636
Silva Aguirre, V., Lund, M. N., Antia, H. M., et al. 2017, ApJ, 835, 173
Siverd, R. J., Beatty, T. G., Pepper, J., et al. 2012, ApJ, 761, 123
Skrutskie, M. F., Cutri, R. M., Stiening, R., et al. 2006, AJ, 131, 1163
Smith, J. C., Stumpe, M. C., Van Cleve, J. E., et al. 2012, PASP, 124, 1000
Somers, G., & Stassun, K. G. 2017, AJ, 153, 101
Song, H. F., Maeder, A., Meynet, G., et al. 2013, A&A, 556, A100
Stassun, K. G., Kratter, K. M., Scholz, A., & Dupuy, T. J. 2012, ApJ, 756, 47
Stassun, K. G., Mathieu, R. D., & Valenti, J. A. 2006, Natur, 440, 311
Stassun, K. G., Oelkers, R. J., Paegert, M., et al. 2019, AJ, 158, 138
Stassun, K. G., Oelkers, R. J., Pepper, J., et al. 2018, AJ, 156, 102
Stumpe, M. C., Smith, J. C., Catanzarite, J. H., et al. 2014, PASP, 126, 100
Stumpe, M. C., Smith, J. C., Van Cleve, J. E., et al. 2012, PASP, 124, 985
Šubjak, J., Sharma, R., Carmichael, T. W., et al. 2020, AJ, 159, 151

Tayar, J., Claytor, Z. R., Huber, D., & van Saders, J. 2022, ApJ, 927, 31
Thorngren, D. P., & Fortney, J. J. 2018, AJ, 155, 214
Thorngren, D. P., Fortney, J. J., Lopez, E. D., Berger, T. A., & Huber, D. 2021, ApJL, 909, L16
Tokovinin, A., Fischer, D. A., Bonati, M., et al. 2013, PASP, 125, 1336
Torra, F., Castañeda, J., Fabricius, C., et al. 2021, A&A, 649, A10
Torres, G. 2013, AN, 334, 4
Triaud, A. H. M. J., Burgasser, A. J., Burdanov, A., et al. 2020, NatAs, 4, 650
Triaud, A. H. M. J., Hebb, L., Anderson, D. R., et al. 2013, A&A, 549, A18
van Saders, J. L., & Pinsonneault, M. H. 2013, ApJ, 776, 67
Vergely, J. L., Lallement, R., & Cox, N. L. J. 2022, A&A, 664, A174
Virtanen, P., Gommers, R., Oliphant, T. E., et al. 2020, NatMe, 17, 261
Vowell, N., Rodriguez, J. E., Quinn, S. N., et al. 2023, AJ, 165, 268
Wenger, M., Ochsenbein, F., Egret, D., et al. 2000, A&AS, 143, 9
Wes McKinney 2010, in Proc. of the 9th Python in Science Conf., ed. C. J. Evans, L. Simard, & H. Takami (Austin, TX: SciPy), 61
West, R. G., Pollacco, D., Wheatley, P., et al. 2016, Msngr, 165, 10
Wittenmyer, R. A., Clark, J. T., Trifonov, T., et al. 2022, AJ, 163, 82
Wright, E. L., Eisenhardt, P. R. M., Mainzer, A. K., et al. 2010, AJ, 140, 1868
Zhou, G., Bakos, G. Á, Bayliss, D., et al. 2019, AJ, 157, 31
Zhou, G., Winn, J. N., Newton, E. R., et al. 2020, ApJL, 892, L21